UC Santa Cruz
UC Santa Cruz Previously Published Works

Title
Targeting the Conserved Stem Loop 2 Motif in the SARS-CoV-2 Genome

Authors
Lulla, Valeria
Wandel, Michal P
Bandyra, Katarzyna J
et al.

Targeting the Conserved Stem Loop 2 Motif in the SARS-CoV-2 Genome

Valeria Lulla,[a] Michal P. Wandel,[b] Katarzyna J. Bandyra,[c] Rachel Ulferts,[d] Mary Wu,[d] Tom Dendooven,[c] Xiaofei Yang,[e] Nicole Doyle,[f] Stephanie Oerum,[g] Rupert Beale,[d] Sara M. O'Rourke,[h] Felix Randow,[b] Helena J. Maier,[f] William Scott,[h] Yiliang Ding,[e] Andrew E. Firth,[a] Kotryna Bloznelyte,[c] Ben F. Luisi[c]

[a]Department of Pathology, Division of Virology, University of Cambridge, Cambridge, United Kingdom
[b]MRC Laboratory of Molecular Biology, Cambridge, United Kingdom
[c]Department of Biochemistry, University of Cambridge, Cambridge, United Kingdom
[d]The Francis Crick Institute, London, United Kingdom
[e]Department of Cell and Developmental Biology, John Innes Centre, Norwich Research Park, Norwich, United Kingdom
[f]Pirbright Institute, Pirbright, Woking, United Kingdom
[g]CNRS-Université Paris Diderot, Institut de Biologie Physico-Chimique, Paris, France
[h]University of California at Santa Cruz, Santa Cruz, California, USA

Valeria Lulla, Michal P. Wandel, Katarzyna J. Bandyra, Rachel Ulferts, Mary Wu, Tom Dendooven, and Xiaofei Yang contributed equally to this work in randomly assigned order.

ABSTRACT RNA structural elements occur in numerous single-stranded positive-sense RNA viruses. The stem-loop 2 motif (s2m) is one such element with an unusually high degree of sequence conservation, being found in the 3' untranslated region (UTR) in the genomes of many astroviruses, some picornaviruses and noroviruses, and a variety of coronaviruses, including severe acute respiratory syndrome coronavirus (SARS-CoV) and SARS-CoV-2. The evolutionary conservation and its occurrence in all viral subgenomic transcripts imply a key role for s2m in the viral infection cycle. Our findings indicate that the element, while stably folded, can nonetheless be invaded and remodeled spontaneously by antisense oligonucleotides (ASOs) that initiate pairing in exposed loops and trigger efficient sequence-specific RNA cleavage in reporter assays. ASOs also act to inhibit replication in an astrovirus replicon model system in a sequence-specific, dose-dependent manner and inhibit SARS-CoV-2 replication in cell culture. Our results thus permit us to suggest that the s2m element is readily targeted by ASOs, which show promise as antiviral agents.

IMPORTANCE The highly conserved stem-loop 2 motif (s2m) is found in the genomes of many RNA viruses, including SARS-CoV-2. Our findings indicate that the s2m element can be targeted by antisense oligonucleotides. The antiviral potential of this element represents a promising start for further research into targeting conserved elements in RNA viruses.

KEYWORDS plus-strand RNA virus, coronavirus, astrovirus, s2m, gapmer, LNA, therapeutic oligonucleotides, SARS-CoV-2

Severe acute respiratory syndrome coronavirus 2 (SARS-CoV-2) is a highly infectious virus and the causative agent of the ongoing coronavirus disease 2019 (COVID-19) pandemic. Given the continued rise in cases worldwide, the significant mortality rate, and the challenges in predicting the severity of illness in infected individuals (1), there is a pressing need for efficacious antiviral therapies (2, 3) (https://www.who.int/emergencies/diseases/novel-coronavirus-2019). Moreover, the potential for further outbreaks of infections by emerging pathogenic coronaviruses (4, 5) places importance on improving fundamental understanding of coronavirus biology, as well as exploring novel therapeutics that could be rapidly repurposed in response to the next zoonotic jump.

Like replication of other positive-sense single-stranded RNA [(+)ssRNA] viruses, replication of SARS-CoV-2 is orchestrated by virus-encoded enzymes inside infected host cells. The 30-kb SARS-CoV-2 genomic RNA and the subgenomic mRNA transcripts all contain a common 5′ leader sequence and a common 3′ UTR, which harbor several conserved structural elements, including the stem-loop 2 motif (s2m) (Fig. 1A and B) (6, 7). The s2m, originally identified in astroviruses (8), is a highly conserved RNA sequence element present within the 3′ UTR in the genomes of many astroviruses, some picornaviruses and noroviruses, and a variety of coronaviruses, including members of the subgenus *Sarbecovirus*, which includes SARS-CoV and SARS-CoV-2 (9, 10). The SARS-CoV and SARS-CoV-2 s2m sequences are nearly identical, with only 2 point nucleotide differences (Fig. 1A), in contrast to the overall 20% genome-wide sequence divergence (7). The s2m sequence is also highly conserved in the clinical isolates from patients that have tested positive for SARS-CoV-2 during the current pandemic, although with a few isolated exceptions (11, 12). The high degree of s2m sequence conservation is likely to be a direct consequence of a requirement to sustain an elaborate three-dimensional structure. Indeed, an earlier study of the SARS-CoV s2m element revealed a stable stem-loop with a few exposed bases (Fig. 1B) in a 2.7-Å-resolution crystal structure (13). Several more recent studies probed RNA accessibility and mapped RNA-RNA interactions of the positive-sense SARS-CoV-2 viral RNAs inside the host cell, confirming that the s2m stem-loop structure folds *in vivo* as well (14, 15).

Because of the apparent high degree of selective pressure to maintain this specific sequence and its structure, the s2m is a promising target for potential antiviral agents, with reduced likelihood of evolving mutations that would lead to resistance. Since the s2m element is present in all positive-sense transcripts (both genomic and subgenomic) produced by a given virus, any agents targeting the s2m would also have the advantage of acting against the majority of viral RNAs present within a cell. In order to test the accessibility of the s2m element to potential nucleic acid-based therapeutics, we designed a panel of antisense oligonucleotides (ASOs). These oligonucleotides have proven therapeutic potential against viruses and have been undergoing active development for more than a decade (16). Third-generation ASOs include locked nucleic acids (LNAs), in which a bicyclic linkage at the furanose constrains the conformational freedom of the nucleotide (17). LNAs provide high-affinity base-pairing to cRNA and DNA targets, as well as resistance to nuclease attack (18). A version of LNA ASOs known as gapmers consist of LNA bases flanking a central DNA sequence (19). In this design, LNA bases confer resistance to nucleases and provide high-affinity base-pairing to the RNA target, while the central DNA region, once base-paired to RNA, recruits RNase H, which acts to cleave the RNA in the RNA-DNA duplex. In this process, the DNA is not digested, and thus, the gapmer remains intact and free to bind further RNA molecules, directing their cleavage. Gapmers have already been successfully used in clinical trials to catalyze the degradation of target transcripts (20).

In this report, we describe the design and testing of several LNA ASOs (gapmers) against the highly conserved structured s2m element from the 3′ UTR of SARS-CoV-2. By performing chemical probing of the RNA, we found that ASOs successfully remodel the s2m structure, despite its high degree of structural compactness. Furthermore, gapmers were capable of inducing sequence-specific RNA cleavage *in vitro* and had an inhibitory effect in multiple independent cell-based platforms, including a human cell reporter system, an astrovirus replicon assay, and SARS-CoV-2 replication in infected cells. Our results support targeting of the s2m element and other conserved structures with predicted exposed loops in viral genomes by ASOs. In addition, the particular gapmer designs described here may offer suitable lead compounds for further development as antiviral therapeutics to treat COVID-19 and other diseases caused by RNA viruses possessing the s2m element in their genomes.

RESULTS

Model for the s2m element in the context of the SARS-CoV-2 3′ UTR. Given the high sequence similarity between the s2m elements in the SARS-CoV-2 and SARS-CoV
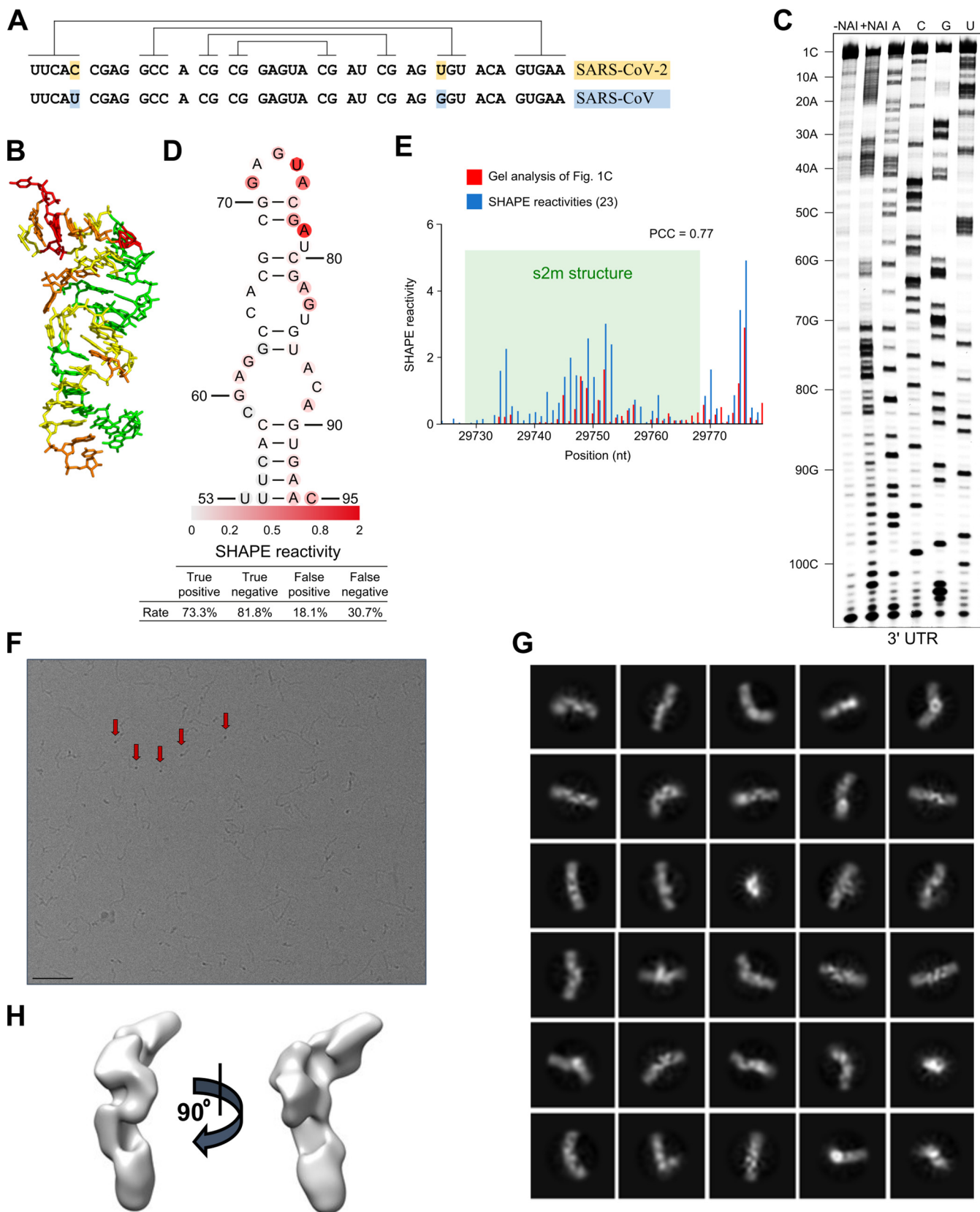
FIG 1 s2m is a conserved structural element in the SARS-CoV-2 genome. (A) Sequence alignment of the *s2m* element in the 3′ UTRs of SARS-CoV-2 and SARS-CoV. Lines indicate base-pairing regions within the element. (B) Crystal structure of the SARS-CoV s2m element (adapted from *PLoS Biology* [13]). (C) SHAPE chemical probing of the 3′ UTR of SARS-CoV-2. RNA was denatured and refolded in the presence of 100 mM K⁺ and 0.5 mM Mg²⁺ and then

(Continued on next page)

genomes (Fig. 1A), the corresponding structures are expected to show high similarity as well, although recent nuclear magnetic resonance (NMR) data suggest some differences in their secondary structures (21).

The crystal structure of the SARS-CoV s2m reveals a stem-loop with a small pocket that can accommodate cations (Fig. 1B) (13) and suggests a similar fold for the SARS-CoV-2 s2m. To test this experimentally, we probed the structure of the SARS-CoV-2 s2m element within the genomic 3′ UTR using SHAPE (selective 2′-hydroxyl acylation analyzed by primer extension) (22). The SHAPE reactivity profile agrees with the crystal structure of the SARS-CoV s2m element (Fig. 1C and D). For instance, high SHAPE reactivities were found at the loop region (G71 to A75), indicating a strong possibility of a single-stranded nature, while low SHAPE reactivities were found for nucleotides predicted to be base-paired, such as nucleotides 54 to 58 and nucleotides 90 to 94 (Fig. 1D). We compared our results from gel-based SHAPE analysis (Fig. 1C) with the previous analyses by Manfredonia et al. (23), performed on the full-length virus genome using SHAPE with mutational profiling (SHAPE-MaP) (Fig. 1E; Table 1). We found an especially high correlation (Pearson correlation coefficient [PCC] = 0.77) between our data and SHAPE-MaP reactivities (Fig. 1E) for the s2m region, indicating that the s2m is an intrinsic structural module. Stable structural unit formation by s2m, maintained within an extended surrounding sequence, was also observed in a recent NMR and dimethyl sulfate (DMS) chemical probing study (21).

To further investigate potential structures formed by the viral 3′ UTR as a whole, we used cryo-electron microscopy (cryo-EM). Imaging this RNA fragment mainly yielded elongated shapes resembling thick rope, up to 500 Å in length (Fig. 1F). A subset of the ropey particles were less extended, measuring around 300 Å, which is about half the length expected for an elongated polymer, implying that the RNA there is semicompact. These particles were subjected to computational 2D/3D averaging in an attempt to reveal underlying shared structural features (Fig. 1G and H). However, none could be clearly identified, suggesting that the 3′ UTR RNA does not fold into a well-defined structure, at least *in vitro*.

Our cryo-electron microscopy observations give support to earlier *in vivo* studies, where cells infected with SARS-CoV-2 virus were probed by cryo-electron tomography (24). Both the tomography study and our single-particle imaging reveal small, high-contrast features at the periphery of the RNA particles, which might represent views down the long axis of some duplex RNA regions (Fig. 1F, red arrows).

Overall, based on the prediction from the SARS-CoV s2m RNA crystal structure and our SHAPE probing results, we conclude that the s2m element in the 3′ UTR of SARS-CoV-2 RNA folds into a stem-loop structure, which may be highly conserved among coronaviruses. This is in contrast to the entire 3′ UTR as a whole, for which we did not observe any well-defined global structure.

Binding and activity of LNA ASO gapmers against the s2m element *in vitro*. Although the highly conserved sequence of the s2m element makes it an attractive target for therapies based on ASOs, the structured nature of the target may potentially interfere with ASO-target base-pairing. To facilitate gapmer-induced disruption of the native s2m structure, we designed gapmers so that the high-affinity LNA bases would pair with the RNA bases predicted to be exposed in the s2m element (Fig. 2 and Table 2). This pairing should facilitate initial gapmer-target interaction, hypothetically leading to unfolding of the s2m element as the rest of the gapmer base-pairs with the complementary target nucleotides.

We designed a panel of gapmers and tested their ability to direct RNase H cleavage *in vitro*, using s2m RNA as the substrate for the purified enzyme (Fig. 2A and D). Different

FIG 1 Legend (Continued)

incubated with NAI (+NAI channel) or DMSO control (−NAI channel). NAI modification was detected by reverse transcription stalling and gel-based analysis. Sequencing lanes were generated by adding ddT (for A), ddG (for C), ddC (for G), and ddA (for U) when reverse transcription was performed. (D) Annotation of SHAPE signal on the s2m structure. (E) Bar plot showing the reactivities of structural profiling of gel-based analysis in our study (C) and in the SHAPE-MaP experiment described by Manfredonia et al. (23). The s2m structure is highlighted by shading in green. (F) Representative cryoEM image of the SARS-CoV-2 3′ UTR (220 nt) at a 2.5-μm defocus. The red arrows indicate features that likely correspond to views along the long axis of duplex regions. Bar, 50 nm. (G) 2D class averages and (H) 3D reconstructions were calculated by cryoSPARC 2.15.0.

TABLE 1 Comparison of s2m SHAPE reactivity data with full SARS-CoV-2 RNA probing in reference 23

| Position (nt) | nt | Reactivity in: | |
		Gel in Fig. 1C	SHAPE-MaP *in vivo* (23)
29724	C	0.0003	0.099
29725	A	0.0011	0.000
29726	U	0.0165	0.160
29727	U	0.0000	0.039
29728	U	0.0000	0.000
29729	U	0.0000	0.037
29730	C	0.0000	0.116
29731	A	0.0025	0.152
29732	C	0.0081	0.000
29733	C	0.0000	0.270
29734	G	0.2168	1.608
29735	A	0.2151	2.273
29736	G	0.2791	0.539
29737	G	0.0000	0.390
29738	C	0.0181	0.110
29739	C	0.0183	0.311
29740	A	0.0284	0.358
29741	C	0.0563	0.237
29742	G	0.0540	0.971
29743	C	0.0370	0.418
29744	G	0.1447	0.642
29745	G	0.8744	1.428
29746	A	0.0845	2.005
29747	G	0.4517	1.473
29748	U	1.4426	1.305
29749	A	1.0879	2.589
29750	C	0.3185	1.423
29751	G	0.7278	0.713
29752	A	1.6490	3.033
29753	U	0.0659	2.408
29754	C	0.1931	0.286
29755	G	0.2435	0.110
29756	A	0.4121	0.475
29757	G	0.5827	0.734
29758	U	0.0173	0.526
29759	G	0.0217	0.059
29760	U	0.1322	0.396
29761	A	0.1796	0.874
29762	C	0.1029	0.157
29763	A	0.3225	0.223
29764	G	0.1078	0.107
29765	U	0.1042	0.124
29766	G	0.1214	0.037
29767	A	0.2554	0.063
29768	A	0.3495	0.043
29769	C	0.5775	0.850
29770	A	0.1371	1.647
29771	A	0.2830	0.470
29772	U	0.5108	0.038
29773	G	0.0684	0.268
29774	C	0.3365	0.870
29775	U	1.2293	3.447
29776	A	2.9140	4.946
29777	G	0.1926	0.496
29778	G	0.1186	0.355
29779	G	0.6380	0.236
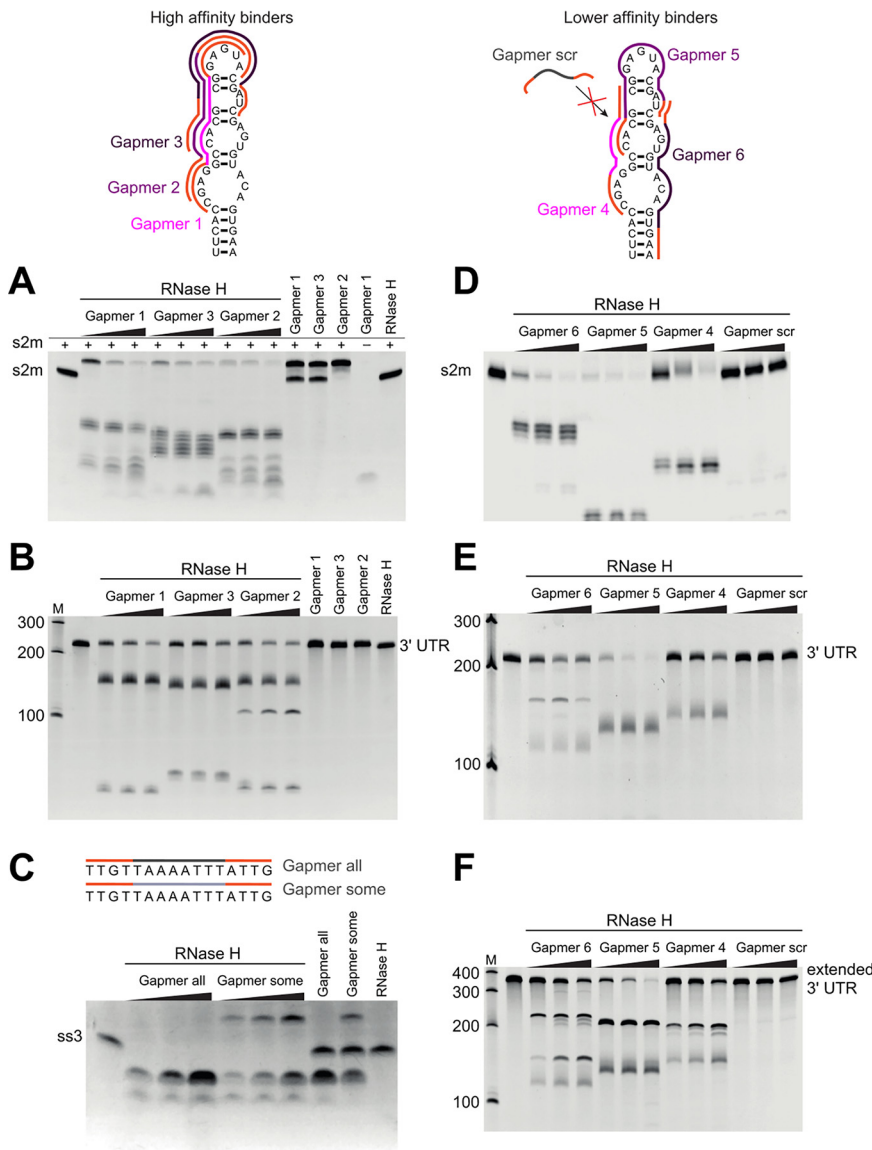
FIG 2 Antisense oligomers direct RNase H cleavage of the s2m element and a conserved single-stranded region (ss3) *in vitro*. (Top) Design of the six gapmers complementary to the s2m, as well as a nonspecific control gapmer "scr" used in this study (Table 3). The LNA is indicated in orange, s2m-specific phosphorothioate-linked DNA in pink/purple, other phosphorothioate-linked DNA in gray ("scr" and "all"), and phosphodiester-linked DNA in light gray ("some"). RNase H cleavage of the isolated s2m (A and D), 3′ UTR (B and E), the extended 3′ UTR (F), and the predicted single-stranded region ss3 (C). Three target-to-gapmer molar ratios were tested: 1:0.5, 1:1, and 1:2. Incubation of RNA target with RNase H alone does not lead to cleavage (RNase H, last lane) and is not driven by control gapmers with scrambled DNA sequence ("scr"). Incubation of RNA target with gapmer without the addition of RNase H does not lead to degradation either, but it does lead to the appearance of a retarded band that likely corresponds to the target-gapmer duplex.

gapmer-target affinities were trialed: gapmers 1 to 3 were designed to have higher affinity for target RNA than gapmers 4 to 6, as indicated by respective predicted melting temperatures (Fig. 2, top, and Table 2). The presence of the sequence-specific gapmers 1 to 6 in the digestion reactions led to clear degradation of the target s2m RNA, regardless of their predicted melting temperature bracket, whereas a non-sequence-specific control gapmer with a scrambled sequence failed to have an effect (Fig. 2D, "Gapmer scr" lanes). The degradation was very efficient even for a 2:1 s2m-to-gapmer molar ratio, indicating that gapmers can be recycled and can direct multiple turnover of substrates by RNase H. Gapmers 1 to 6 also drove cleavage of the whole 3′ UTR (Fig. 2B and E) and of the

TABLE 2 Gapmers used in this study

Gapmer	Sequence[a]	T_m (°C)[b]	
		DNA	RNA
1	[+A]*[+C]*[+T]*[+C]*C*G*C*G*T*G*G*C*[+C]*[+T]*[+C]*[+G]	85	93
2	[+T]*[+A]*[+C]*[+T]*C*C*G*C*G*T*G*G*[+C]*[+C]*[+T]*[+C]	81	97
3	[+G]*[+A]*[+T]*[+C]*G*T*A*C*T*C*C*G*[+C]*[+G]*[+T]*[+G]	78	88
4	[+G]*[+C]*G*T*G*G*C*C*[+T]*[+C]*[+G]	69	76
5	[+G]*[+A]*T*C*G*T*A*C*T*C*C*G*C*[+G]*[+T]*[+G]	70	76
6	[+T]*[+T]*[+C]*A*C*T*G*T*A*C*A*C*T*[+C]*[+G]*[+A]	68	79
scr	[+A]*[+C]*C*G*T*G*C*G*G*T*A*T*T*[+C]*[+G]*[+C]	71	75
all	[+C]*[+A]*[+A]*[+T]*A*A*A*T*T*T*T*A*[+A]*[+C]*[+A]*[+A]	53	50
some	[+C]*[+A]*[+A]*[+T]AAATTTTA[+A]*[+C]*[+A]*[+A]	53	50

[a]*, phosphorothioate backbone linkage; [+X], LNA base X.
[b]Melting temperature predictions were obtained using an online oligonucleotide design tool (Qiagen).

extended 3′ UTR construct, which additionally includes open reading frame 10 (ORF10) and the region immediately upstream of it (Fig. 2F; Table 3), indicating that the target s2m sequence is successfully recognized and is accessible for gapmer base-pairing in the context of the longer 3′ UTR. The observation that both the higher-affinity gapmers 1 to 3 (Fig. 2A and B) and the lower-affinity gapmers 4 to 6 (Fig. 2 D to F) were able to direct RNase H cleavage of the s2m element indicates that a range of gapmer-target affinities are compatible with successful target degradation of the highly structured s2m sequence. This flexibility in gapmer design is particularly encouraging for potential development of therapeutics, as lower-affinity gapmers may be expected to have fewer off-target interactions in cells than the higher-affinity variants.

Additionally, we designed and tested gapmers targeting a single-stranded conserved region in SARS-CoV-2, at positions 1359 to 1374 relative to the virus reference genome (known as ss3; GenBank no. NC_045512.2) (6) and tested alternative gapmer backbone chemistries with these. Gapmers designated "all" and "some" have the same sequence and base composition but different polymer backbones (Table 2). The entire backbone of gapmer "all" contains phosphorothioate modifications, as is also the case

TABLE 3 Sequences of RNAs used in this study

Description	Sequence[a]
SARS-CoV-2 s2m sequence used in RNase H assays *in vitro* and in GFP reporter assays (47 nt)	GGAG**UUCACCGAGGCCACGCGGAGUACGAUCGAGUGUACAGUGAA**UU
Scrambled control sequence used in GFP reporter assays (47 nt)	AGCCGGGCUGGAAGAUACUGCCCAAAUAGGGAACUUUGACGCGGUUG
SARS-CoV-2 3′ UTR (220 nt)	UAGCAAUCUUUAAUCAGUGUGUAACAUUAGGGAGGACUUGAAAGAGCC ACCACAUU**UUCACCGAGGCCACGCGGAGUACGAUCGAGUGUACAGUGAA** CAAUGCUAGGGAGAGCUGCCUAUAUGGAAGAGCCCUAAUGUGUAAAA UUAAUUUUAGUAGUGCUAUCCCCAUGUGAUUUUAAUAGCUUCUUAGGAGAA UGACAAAAAAAAAAAAAAAAAAAAAAA
SARS-CoV-2 extended 3′ UTR (358 nt)	ACUCAUGCAGACCACACAAGGCAGAUGGGCUAUAUAAACGUUUUCGCUUUU CCGUUUACGAUAUAUAGUCUACUCUUGUGCAGAAUGAAAUUCUCGUAACUA CAUAGCACAAGUAGAUGUAGUUAACUUUUAAUCUCACAUAGCAAUCUUUAAU CAGUGUGUAACAUUAGGGAGGACUUGAAAGAGCCACCACAUU**UUCACCGAG GCCACGCGGAGUACGAUCGAGUGUACAGUGAA**CAAUGCUAGGGAGAGCU GCCUAUAUGGAAGAGCCCUAAUGUGUAAAAUUAAUUUUAGUAGUGCUAU CCCCAUGUGAUUUUAAUAGCUUCUUAGGAGAAUGACAAAAAAAAAAAAAAA AAAAAAAA
SARS-CoV-2 ss3 (16 nt). A conserved region predicted to be single-stranded in the genome; positions 1359–1374 relative to the NC_045512.2 reference (6)	UUGUUAAAAUUUAUUG

[a]Boldface indicates the extended s2m region common to these RNA substrates.

in gapmers 1 to 6; it is a well-established modification conferring some nuclease resistance to oligonucleotides (25, 26). The backbone in gapmer "some," however, is mixed; DNA bases are linked by a phosphodiester backbone, whereas LNA bases are linked by a phosphorothioate backbone.

In vitro digestion experiments (Fig. 2C) indicate that both chemistries are compatible with RNase H recruitment and the degradation of the RNA target and also suggest general applicability of gapmer-directed cleavage of virus RNA sequences. Gapmer "some" appears to have higher binding affinity for the ss3 target, judging from the presence of an extra band at the top of the gel in Fig. 2C, which likely corresponds to a gapmer-target dimer. This is consistent with expectation, as phosphorothioate modifications are known to reduce target affinity (27), so gapmer "all" would be expected to show weaker binding than gapmer "some." On the other hand, gapmer "all" generates a larger amount of cleaved product (Fig. 2C), which supports our choice of a phosphorothioate backbone throughout gapmers 1 to 6.

**Despite being structured, the s2m is successfully remodeled by LNA gapmers.** To confirm that gapmers affect the s2m structure, we performed SHAPE probing of the SARS-CoV-2 3′ UTR in the presence of gapmers 1, 2, and 3 targeting s2m and gapmer "all" as a nonspecific control. Since SHAPE probing detects the accessibility of nucleotides (22), it is capable of revealing both intra- and intermolecular RNA base-pairing interactions.

In the presence of gapmer 1, SHAPE reactivity profiles strongly decreased in the gapmer-targeted region from G60 to C69 (Fig. 3A and B), indicating successful gapmer-target base-pairing. Due to the interaction between the gapmer and its target site, the other arm of the s2m (U79 to A94) loses base-pairing interactions and becomes more single-stranded, as evidenced by a strong increase in SHAPE reactivity in this region (Fig. 3A and B). We also found slightly decreased SHAPE reactivities in the region from A75 to A78 and increased SHAPE reactivities in the region from G70 to A75. The latter might be due to a dynamic interaction between the 3′ end of the gapmer and the target site or due to conformational remodeling leading to a higher accessibility of the SHAPE reagent to the 2′-OH of these nucleotides. Similar changes in SHAPE reactivities were also observed in the presence of gapmer 2 (Fig. 3C and D), which targets s2m with a 1-nucleotide (nt) shift compared to the target site of gapmer 1 (G60 to C76 and C59 to A75, respectively).

In the presence of gapmer 3, which targets the single-stranded loop region within s2m, the SHAPE reactivity profile showed a strong decrease in the region from G60 to A75 (Fig. 3E and F), indicating successful base-pairing interactions with the gapmer. We also found that this intermolecular interaction between gapmer 3 and the loop region led to increased SHAPE reactivities downstream of the loop region. Thus, the intermolecular interactions between gapmers and target regions could also remodel the folding status of flanking regions.

Notably, the observed changes in SHAPE reactivity were dependent on the concentration of gapmers and were not detected in the presence of a control gapmer (gapmer "all") which is not able to target the s2m element (Fig. 3G and H). Taken together, our results validate the design of gapmers to target the s2m element and highlight the effect of gapmers in remodeling the s2m structure to gain access to a highly structured RNA.

s2m induces gapmer-directed reduction of reporter gene expression in human cells. To investigate if gapmers against the s2m element could drive target RNA degradation in human cells, we set up a tissue culture-based reporter system. We generated lung-derived A549 and HeLa cell reporter lines carrying stably integrated GFP genes that encode either the wild type s2m element or a scrambled control sequence in their 3′ UTR (Fig. 4A to C). Transfection with gapmers against s2m reduced GFP fluorescence levels in the two s2m-containing cell lines for both the higher-affinity gapmers (gapmers 1 to 3) and the lower-affinity gapmers (gapmers 5 to 6) (Fig. 4D and F). Gapmer 4, which is the shortest of the tested gapmers and contains only six DNA nucleotides (Table 2), had no effect (Fig. 4D and F); this may reflect difficulties in recruiting human RNase H *in vivo* to this length of RNA-DNA duplex (28). Nonspecific control
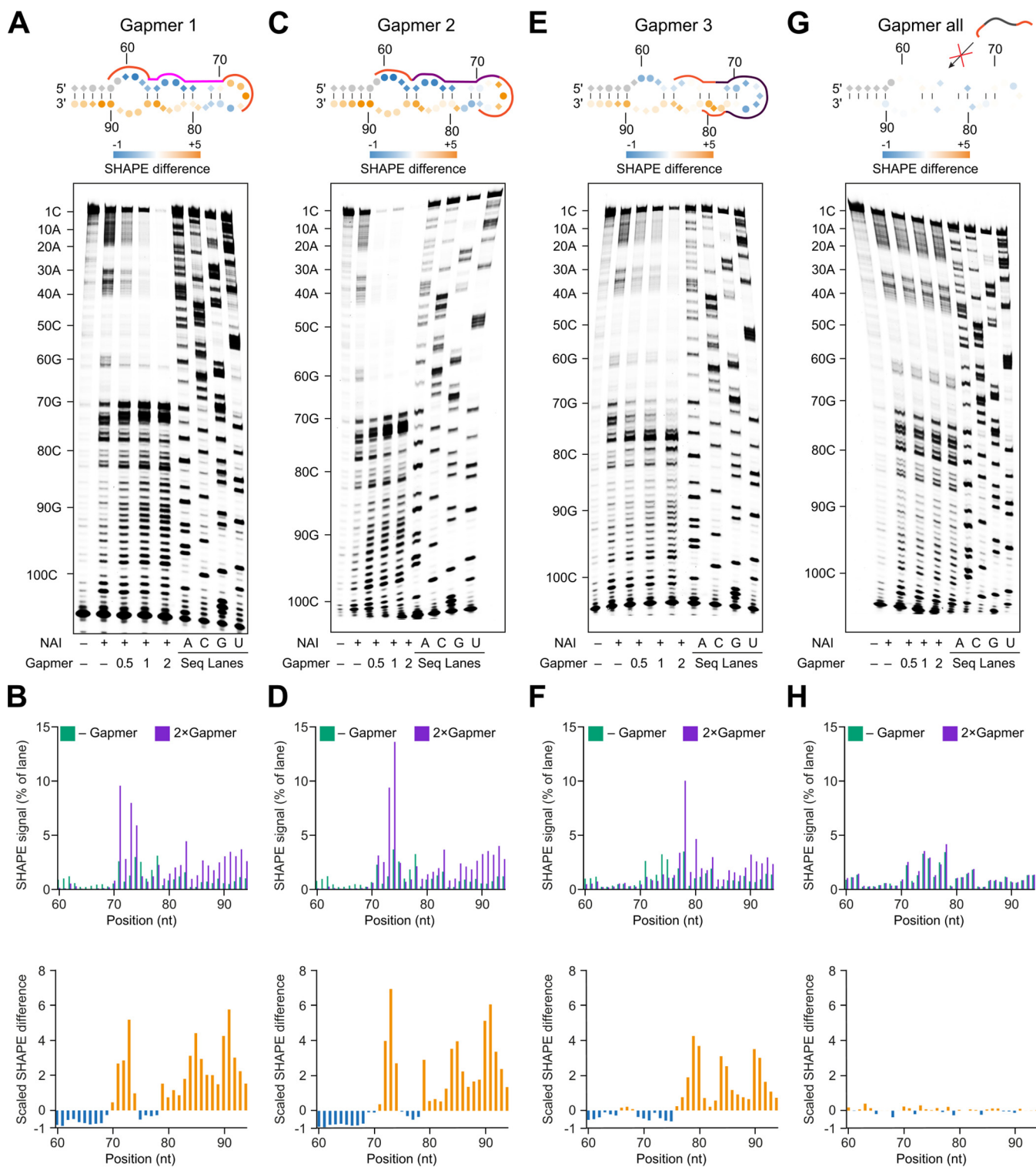
FIG 3 SHAPE probing reveals RNA structure changes induced by LNA gapmers. (A, C, E, and G) SHAPE probing of SARS-CoV-2 3′ UTR structure in the presence or absence of the gapmer indicated. RNA was denatured and refolded in the presence of 100 mM K⁺ and 0.5 mM Mg²⁺, then incubated with different gapmer-to-target molar ratios (0, 0.5, 1, and 2), and probed using NAI. (B, D, F, and H) Quantification of results in panels A, C, E, and G, respectively. Analysis of the differences in SHAPE signal from SARS-CoV-2 3′ UTR alone and in the presence of 2× molar excess of the gapmer. (A and B) The presence of gapmer 1 induced an increase in SHAPE signal at positions 70 to 74 and 79 to 94 (highlighted in orange), indicating that these nucleotides are more unstructured. A strong decrease in SHAPE signal was observed at positions 60 to 69 (highlighted in blue), indicating decreased accessibility of these bases, which could be caused by their base-pairing with the gapmer. (C and D) The reactivity profile in D is similar to that in B, due to the similar target regions of gapmer 1 and gapmer 2. (E and F) In the presence of gapmer 3, nucleotides at positions 69 to 75 are more structured, while nucleotides at positions 76 to 94 are less structured, as indicated. (G and H) No significant differences in SHAPE signal could be detected in the presence or absence of the nonspecific control gapmer "all," indicating that it is unable to cause structural changes in the SARS-CoV-2 3′ UTR.
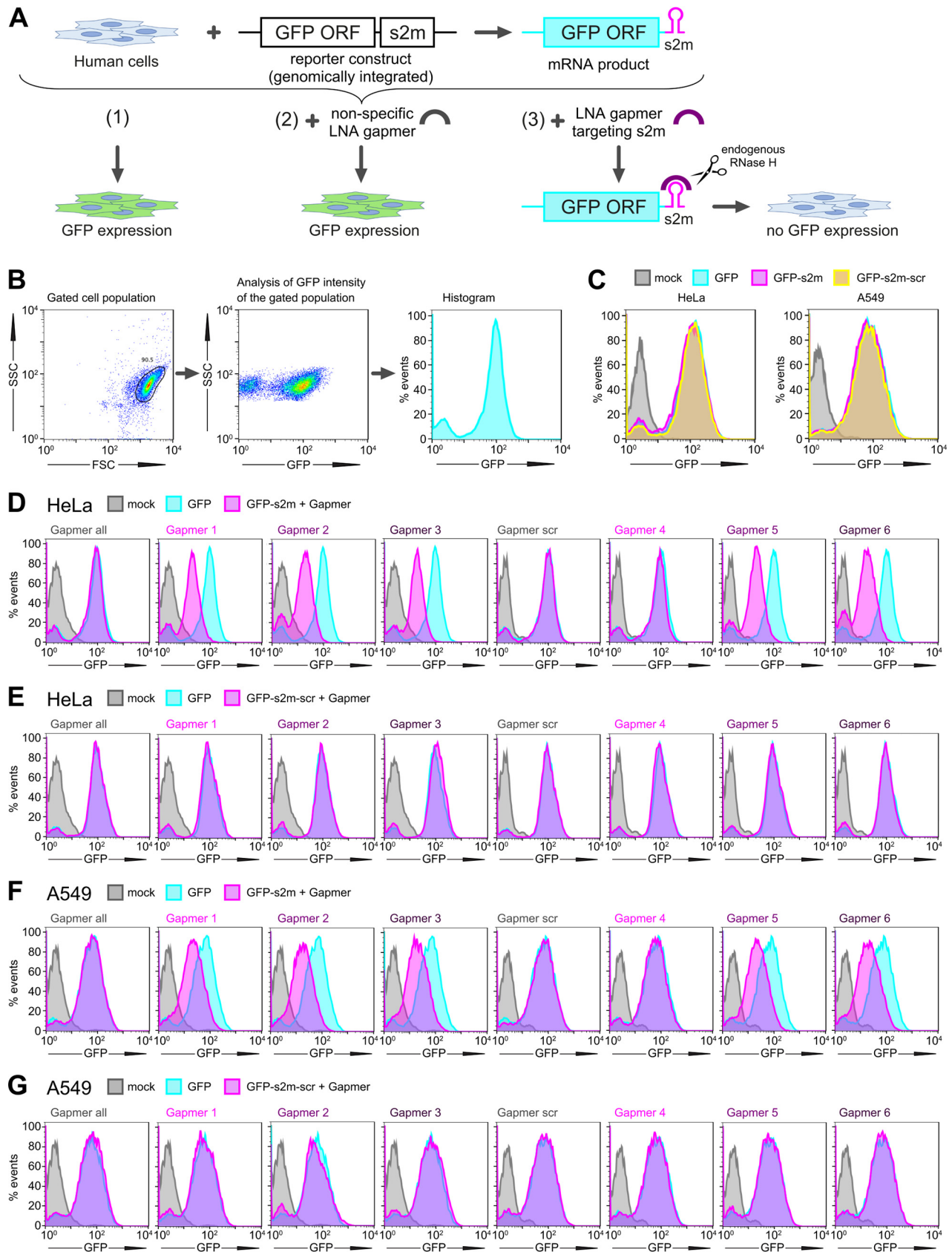
FIG 4 Gapmer-induced reduction of protein levels in cell reporter assays. (A) Schematic of the GFP reporter assay. (B) Gating and data visualization strategy of the reporter assay data. The main cell population was identified and gated on forward and side scatter using the Auto Gate tool and

(Continued on next page)

gapmers did not affect GFP fluorescence levels, nor did treatment with s2m-specific gapmers of control cell lines in which the sequence of the s2m element was scrambled (Fig. 4E and G). These results indicate that the gapmer-mediated reduction in target gene expression relies on sequence-specific gapmer-target interaction. Overall, the results indicate that gapmers against the s2m element have the potential to decrease gene expression from mRNAs containing s2m in their 3′ UTR sequences, which is the case for SARS-CoV-2 mRNAs.

Our experimental method was also used to test the hypothesis that the s2m is a posttranscriptional response element. We used the green fluorescent protein (GFP) reporter cell lines to compare fluorescence levels between the GFP-s2m and GFP-scrambled cells. No difference was observed, indicating that the s2m element itself does not affect fluorescent-protein production (Fig. 4C), which suggests that it does not act as an independent element in *cis* in translation or stability of viral mRNAs.

LNA gapmers against s2m inhibit replication in an astrovirus replicon model system in human cells. To investigate the effects of s2m-targeting LNA gapmers on viral replication, initially we employed an astrovirus replicon system, where the measured luciferase signal represents the translation of a reporter protein from subgenomic RNAs. Many (+)ssRNA viruses share a similar repertoire of genetic elements required for the replication of viral RNA, and this is true in the case of coronaviruses and astroviruses. Despite a large disparity in genome size, coronaviruses and astroviruses possess a similar modular organization, with a largely similar ordering of nonstructural and structural genes, a frameshift signal to access the open reading frame encoding the RNA-dependent RNA polymerase (RdRp), and production of 3′-coterminal subgenomic mRNAs for structural and accessory protein expression. Like coronaviruses, many astroviruses—including human astrovirus 1 (HAstV1)—contain an s2m element in the 3′ UTR of their genomes (Fig. 5A). We recently developed a robust HAstV1-based replicon system (Fig. 5A, bottom) which permits the evaluation of RNA replication in multiple cell types (29). The small astrovirus genome (~7 kb), in contrast to the much larger coronaviruses (~30 kb), allows rapid manipulation of sequences for antiviral testing in a less restrictive environment than that required to manipulate SARS-CoV-2.

Building on promising results in the cell-based reporter system, we used the astrovirus system to test gapmer efficacy in the context of virus-like replication, where replicative intermediates are generally physically occluded within host membrane-derived vesicles, as is also the case in bona fide virus infection. We generated chimeric astrovirus replicons bearing the s2m elements from SARS-CoV or SARS-CoV-2 (Fig. 5B). Chimeric replicons recapitulated the replication properties of the wild-type astrovirus replicon (Fig. 5C), indicating that this system is suitable for testing gapmers against multiple s2m sequences. To rule out any potential cell-specific effects, all gapmers were tested in two human cell lines, Huh7.5.1 (29) and HEK293T (optimized for this study). The replication of replicons bearing SARS-CoV-2 s2m sequences was efficiently inhibited by gapmers 1, 2, and 5, causing inhibition in the subnanomolar range, with a less pronounced effect found for gapmers 3, 4, and 6. The inhibition of nonspecific control gapmers ("all" and "scr") was significantly below that of their composition-matched counterparts, gapmers 1 to 3 and 4 to 6, respectively (Fig. 5D; Table 4). The same gapmers were also tested against the SARS-CoV s2m in this system and found to be active, though with a lower potency (Fig. 5E; Table 5). This could potentially be

FIG 4 Legend (Continued)

plotted as a histogram to visualize GFP intensity of cells. (C) HeLa and A549 cells containing a genomic insertion of a GFP reporter construct without additional insertion in its 3′ UTR (GFP), with the s2m sequence in its 3′ UTR (GFP-s2m), or with a scrambled sequence insertion in its 3′ UTR (GFP-s2m-scr) were analyzed by flow cytometry. Data are representative of two independent experiments. (D to G) Flow cytometry analysis of the GFP-expressing cells. HeLa (D) and A549 (F) cells containing a genomic insertion of a GFP reporter construct with the s2m sequence in its 3′ UTR (GFP-s2m) were transfected with a 20 nM concentration of the indicated gapmers and analyzed 72 h posttransfection by flow cytometry. Treatment with gapmers against the s2m element, but not a nonspecific control gapmer, induced reduction in fluorescence. HeLa (E) and A549 (G) cell lines containing a control genomic insertion of a GFP reporter construct with a scrambled sequence inserted in its 3′ UTR (GFP-s2m-scr) were transfected with 20 nM the indicated gapmers and analyzed 72 h posttransfection by flow cytometry. The control cell lines containing GFP reporter with a scrambled sequence insertion in the 3′ UTR show no appreciable change in fluorescence upon treatment with the gapmers targeted against the s2m element. Data are representative of three independent experiments (D to G).
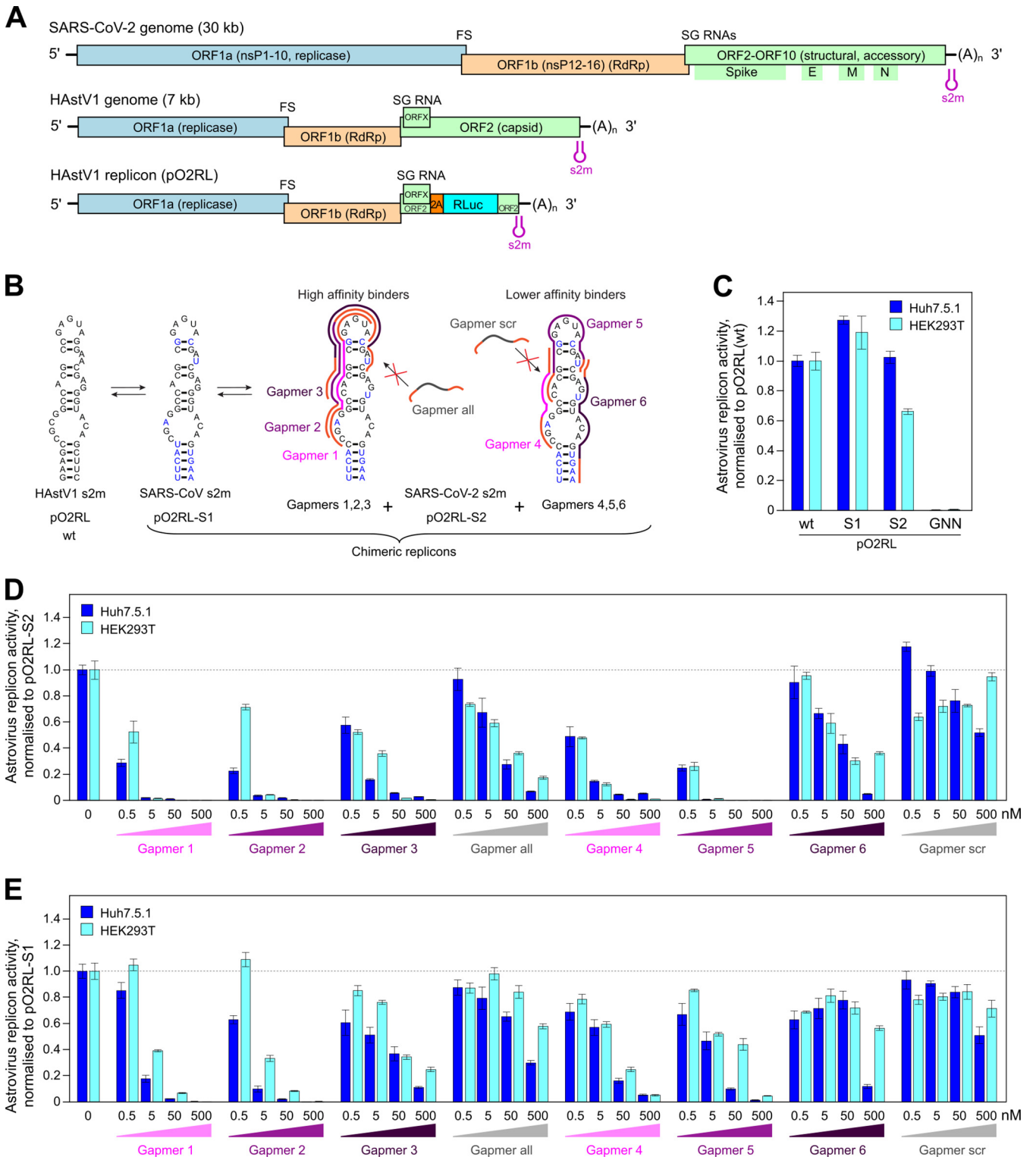
FIG 5 Inhibition of astrovirus replicon activity by gapmers targeting the SARS-CoV-2 s2m RNA element. (A) Schematic of the SARS-CoV-2 and human astrovirus 1 (HAstV1) genome organization. The lowest panel represents the astrovirus replicon (pO2RL). FS, frameshift signal; SG, subgenomic; RLuc, *Renilla* luciferase; RdRp, RNA-dependent RNA polymerase. The presented virus and replicon genomes are not to scale. (B) Conservation of the s2m 3′ UTR element (two-dimensional representation) between HAstV1, SARS-CoV, and SARS-CoV-2. In the astrovirus replicon, the HAstV1 s2m was switched for the SARS-CoV or SARS-CoV-2 s2m; the wild-type and chimeric replicons are indicated below. Gapmers 1, 2, and 3 and gapmers 4, 5, and 6 are color coded in light, medium, and dark magenta, respectively. (C) Luciferase activity of the wild-type, chimeric, and replication-deficient (RdRp GDD motif mutated to GNN) astrovirus replicons measured in Huh7.5.1 (dark blue bars) and HEK293T (light blue bars) cells. (D) Inhibition of the astrovirus chimeric replicon containing the SARS-CoV-2 s2m by gapmers at a 0.5 to 500 nM concentration range. (E) Inhibition of the astrovirus chimeric replicon containing SARS-CoV s2m by gapmers at a 0.5 to 500 nM concentration range. For panels D to E, data are means ± standard deviations (SD) from 3 biologically independent experiments; full data and statistical analyses are provided in Tables 4 and 5. Replicon activity is presented as the ratio of *Renilla* (subgenomic reporter) to firefly (cap-dependent translation, loading control) luciferase activity, normalized by the same ratio for the untreated control replicon.

TABLE 4 Statistical analysis for the inhibition assay of chimeric astrovirus replicon containing SARS-CoV-2 s2m[a]

Cells		Huh7.5.1					HEK293T				
Sample	Conc. μM	Mean fold	s.d.	P-value [S2S]	P-value [control gapmer]		Mean fold	s.d.	P-value [S2S]	P-value [control gapmer]	
pO2RL-S2S	0	1.0000	0.0362	ref	n/a		1.0004	0.0704	ref	n/a	
+ Gapmer 1	0.5	0.2900	0.0288	0.00002	0.0031	1	0.5280	0.0842	0.00196	0.0471	1
	5	0.0218	0.0022	0.00044	0.0094	2	0.0160	0.0022	0.00169	0.0006	2
	50	0.0121	0.0027	0.00042	0.0060	3	0.0013	0.0001	0.00165	0.0003	3
	500	0.0023	0.0006	0.00044	0.0011	4	0.0014	0.0001	0.00165	0.0019	4
+ Gapmer 2	0.5	0.2273	0.0216	0.00004	0.0033	1	0.7145	0.0205	0.01400	0.2231	1
	5	0.0367	0.0044	0.00040	0.0098	2	0.0426	0.0002	0.00180	0.0008	2
	50	0.0197	0.0016	0.00044	0.0065	3	0.0051	0.0006	0.00166	0.0003	3
	500	0.0032	0.0001	0.00044	0.0014	4	0.0020	0.0003	0.00165	0.0019	4
+ Gapmer 3	0.5	0.5767	0.0618	0.00144	0.0061	1	0.5235	0.0197	0.00451	0.0002	1
	5	0.1591	0.0077	0.00037	0.0147	2	0.3597	0.0210	0.00215	0.0004	2
	50	0.0564	0.0034	0.00044	0.0085	3	0.0184	0.0012	0.00171	0.0002	3
	500	0.0291	0.0018	0.00045	0.0011	4	0.0060	0.0003	0.00167	0.0020	4
+ Gapmer all	0.5	0.9289	0.0864	0.28993	ref 1		0.7358	0.0144	0.01937	ref 1	
	5	0.6728	0.1103	0.02648	ref 2		0.5923	0.0263	0.00482	ref 2	
	50	0.2759	0.0363	0.00002	ref 3		0.3624	0.0101	0.00347	ref 3	
	500	0.0678	0.0041	0.00043	ref 4		0.1747	0.0132	0.00181	ref 4	
+ Gapmer 4	0.5	0.4892	0.0744	0.00204	0.0009	5	0.4808	0.0074	0.00564	0.0072	5
	5	0.1472	0.0064	0.00043	0.0006	6	0.1241	0.0110	0.00174	0.0012	6
	50	0.0467	0.0050	0.00038	0.0048	7	0.0087	0.0003	0.00168	0.0001	7
	500	0.0538	0.0058	0.00036	0.0010	8	0.0114	0.0009	0.00168	0.0004	8
+ Gapmer 5	0.5	0.2477	0.0226	0.00003	0.0000	5	0.2607	0.0301	0.00083	0.0001	5
	5	0.0083	0.0015	0.00043	0.0006	6	0.0134	0.0014	0.00169	0.0014	6
	50	0.0006	0.0000	0.00044	0.0043	7	0.0011	0.0000	0.00165	0.0001	7
	500	0.0008	0.0001	0.00044	0.0012	8	0.0012	0.0001	0.00165	0.0004	8
+ Gapmer 6	0.5	0.9037	0.1248	0.31172	0.0542	5	0.9549	0.0280	0.38466	0.0002	5
	5	0.6675	0.0378	0.00039	0.0005	6	0.5919	0.0771	0.00255	0.0815	6
	50	0.4311	0.0738	0.00144	0.0078	7	0.3026	0.0254	0.00133	0.0003	7
	500	0.0502	0.0045	0.00040	0.0011	8	0.3622	0.0107	0.00341	0.0003	8
+ Gapmer scr	0.5	1.1758	0.0355	0.00388	ref 5		0.6406	0.0284	0.00604	ref 5	
	5	0.9914	0.0404	0.79653	ref 6		0.7211	0.0454	0.00716	ref 6	
	50	0.7626	0.0868	0.02795	ref 7		0.7276	0.0105	0.01966	ref 7	
	500	0.5190	0.0305	0.00007	ref 8		0.9490	0.0322	0.33904	ref 8	
pO2RL-GNN	0	0.0014	0.0001	0.00044	n/a		0.0039	0.0002	0.00166	n/a	

[a]P values are from two-tailed t tests with separate variances; "ref" represents the reference data set for each calculation. The color scheme green-yellow-red represents least-to-most inhibited samples.

attributed to differences arising from C-G versus C-U juxtaposition within the respective s2m elements (Fig. 5B) (30), potentially affecting the s2m gapmer binding properties. Replication in the presence of sufficient concentrations of gapmers 1, 2, or 5 dropped to the baseline level of the pO2RL-GNN mutant (Tables 4 and 5), which is completely deficient in replication due to a mutated RdRp active site (Fig. 5C).

To assess the cytotoxicity and potential off-target effects of the tested gapmers, we (i) performed a lactate dehydrogenase (LDH) release-based cytotoxicity assay and (ii) evaluated the efficiency of cap-dependent translation in the presence of the different gapmer concentrations. Consistent with previous work (31), these assays showed no gapmer-induced cellular toxicity (Fig. 6A). Translation inhibition of > 50% was observed only at 500 nM concentrations of gapmers 1, 2, 5 and 6 (Fig. 6B), which is at least 10-fold higher than the effective inhibition range for gapmers 1, 2 and 5. Overall, these results suggest that gapmers targeting the s2m element can inhibit viral replication in the model replicon system in a dose-dependent, sequence-specific manner without causing significant cell toxicity.

SARS-CoV-2 growth is inhibited by LNA gapmers targeting s2m. A high-content screening (HCS) assay was developed to measure the effects of LNA gapmers on infection in Vero E6 cells infected with SARS-CoV-2. Figure 7A shows a graphical representation of the HCS assay workflow and a representative microscopy image, with cells

TABLE 5 Statistical analysis for the inhibition assay of chimeric astrovirus replicon containing SARS-CoV s2m[a]

Cells		Huh7.5.1					HEK293T				
Sample	Conc. µM	Mean fold	s.d.	P-value [S1S]	P-value [control gapmer]		Mean fold	s.d.	P-value [S1S]	P-value [control gapmer]	
pO2RL-S1S	0	1.0000	0.0545	ref	n/a		1.0000	0.0623	ref	n/a	
+ Gapmer 1	0.5	0.8509	0.0604	0.03426	0.6572	1	1.0472	0.0453	0.35359	0.0074	1
	5	0.1771	0.0263	0.00022	0.0038	2	0.3910	0.0099	0.00287	0.0015	2
	50	0.0241	0.0002	0.00104	0.0010	3	0.0683	0.0041	0.00143	0.0012	3
	500	0.0024	0.0005	0.00099	0.0012	4	0.0019	0.0002	0.00130	0.0004	4
+ Gapmer 2	0.5	0.6292	0.0334	0.00135	0.0067	1	1.0877	0.0541	0.14094	0.0064	1
	5	0.0985	0.0243	0.00022	0.0031	2	0.3316	0.0248	0.00091	0.0002	2
	50	0.0211	0.0014	0.00103	0.0010	3	0.0838	0.0032	0.00150	0.0013	3
	500	0.0018	0.0004	0.00099	0.0012	4	0.0035	0.0003	0.00130	0.0004	4
+ Gapmer 3	0.5	0.6064	0.0964	0.00738	0.0217	1	0.8500	0.0385	0.03223	0.5561	1
	5	0.5098	0.0595	0.00048	0.0131	2	0.7614	0.0152	0.01747	0.0100	2
	50	0.3686	0.0543	0.00014	0.0031	3	0.3413	0.0187	0.00149	0.0010	3
	500	0.1088	0.0090	0.00096	0.0005	4	0.2475	0.0171	0.00123	0.0000	4
+ Gapmer all	0.5	0.8741	0.0582	0.05250	ref 1		0.8704	0.0396	0.04772	ref 1	
	5	0.7915	0.0870	0.03247	ref 2		0.9786	0.0476	0.66236	ref 2	
	50	0.6496	0.0348	0.00152	ref 3		0.8390	0.0480	0.02656	ref 3	
	500	0.2983	0.0176	0.00084	ref 4		0.5776	0.0198	0.00398	ref 4	
+ Gapmer 4	0.5	0.6876	0.0649	0.00342	0.0111	5	0.7841	0.0373	0.01146	0.8771	5
	5	0.5680	0.0599	0.00079	0.0062	6	0.5916	0.0205	0.00414	0.0006	6
	50	0.1602	0.0190	0.00047	0.0003	7	0.2470	0.0174	0.00120	0.0016	7
	500	0.0527	0.0040	0.00104	0.0064	8	0.0503	0.0060	0.00131	0.0029	8
+ Gapmer 5	0.5	0.6684	0.0822	0.00664	0.0141	5	0.8532	0.0103	0.05175	0.0614	5
	5	0.4641	0.0680	0.00056	0.0050	6	0.5175	0.0132	0.00410	0.0006	6
	50	0.0988	0.0074	0.00102	0.0009	7	0.4381	0.0464	0.00037	0.0009	7
	500	0.0130	0.0015	0.00101	0.0055	8	0.0449	0.0019	0.00140	0.0030	8
+ Gapmer 6	0.5	0.6259	0.0688	0.00218	0.0055	5	0.6856	0.0061	0.01223	0.0428	5
	5	0.7125	0.0769	0.00817	0.0425	6	0.8100	0.0509	0.01622	0.8267	6
	50	0.7758	0.0681	0.01249	0.2694	7	0.7181	0.0469	0.00424	0.0490	7
	500	0.1180	0.0141	0.00068	0.0068	8	0.5621	0.0169	0.00426	0.0477	8
+ Gapmer scr	0.5	0.9305	0.0682	0.24332	ref 5		0.7792	0.0361	0.01099	ref 5	
	5	0.9049	0.0189	0.08136	ref 6		0.8021	0.0271	0.01881	ref 6	
	50	0.8373	0.0435	0.01717	ref 7		0.8405	0.0579	0.03174	ref 7	
	500	0.5072	0.0642	0.00061	ref 8		0.7127	0.0642	0.00514	ref 8	
pO2RL-GNN	0	0.0012	0.0001	0.00099	n/a		0.0032	0.0004	0.00130	n/a	

[a]P values are from two-tailed t tests with separate variances; "ref" represents the reference data set for each calculation. The color scheme green-yellow-red represents least-to-most inhibited samples.

stained for N protein (488-nm signal). We tested gapmers 1 to 6, "all," and "scr" at 0.25 µM, 0.5 µM, and 1 µM concentrations, alongside a no-gapmer treatment as a negative control and a 10 µM remdesivir treatment as a positive control. Our results indicate that gapmers 2 and 5 inhibit SARS-CoV-2 infection in a dose-dependent manner. At the 1 µM concentration, these gapmers reduced virus replication (measured through N protein expression) to 10.4% and 6.9% of the no-gapmer control, respectively, with cell viability at 72% and 83%, respectively. Furthermore, these inhibition levels are comparable to that of the 10 µM remdesivir control in this assay (Fig. 7B). Gapmers 1, 3, and 6 had a less profound effect (27%, 31%, and 17% of nontreated control levels at 1 µM), whereas gapmer 4 showed the highest toxicity levels (54% viability) besides inhibition to 13% of the nontreated control. In strong agreement with the astrovirus replicon-based results (Fig. 5D), gapmers 2 and 5 demonstrated the most promising results in SARS-CoV-2 inhibition assays (Fig. 7B), suggesting that these two gapmers could be preferred for therapeutic development. Consistent with our previous results on other cell lines (Fig. 6A), the gapmers show no cytotoxic effect on Vero E6 cells in the absence of transfection reagent (<5%) (Fig. 7C), providing further confidence for potential therapeutic gymnotic delivery (32). These results are consistent with the results from the astrovirus replicon system and indicate that gapmers may have sufficient access to their RNA targets to direct degradation in infected cells and
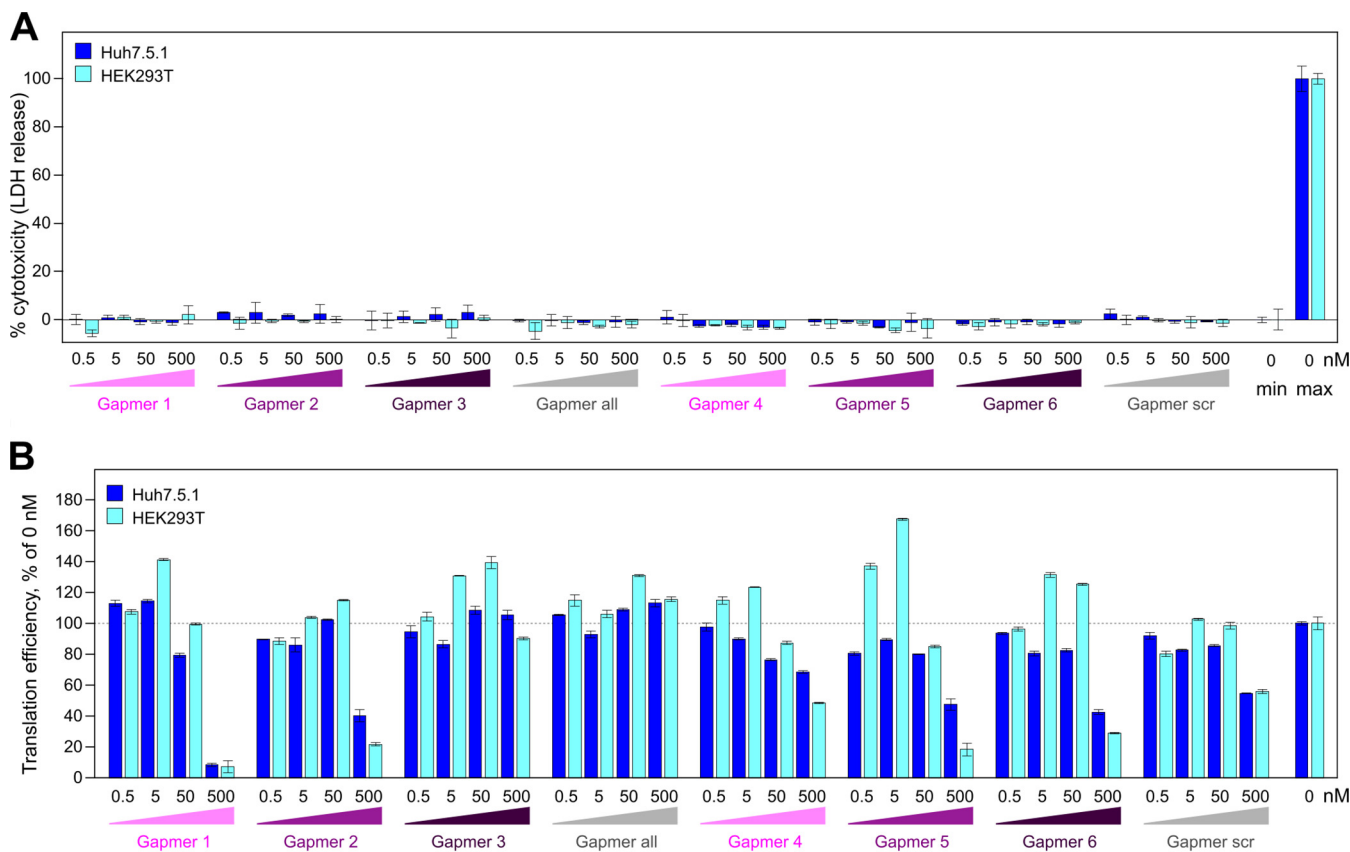
FIG 6 Testing the cytotoxic and off-target effects of gapmers. (A) Toxicity assay for gapmer-treated cells. Cells were treated with 0.5 to 500 nM gapmers for 24 h. Supernatant was used to measure cell viability, calculated as the ratio of released to total lactate dehydrogenase (LDH) activity; "max" refers to the maximum LDH measured for fully lysed cells. (B) Effect on translation measured as a readout of capped T7 RNA encoding firefly luciferase at a 0.5 to 500 nM gapmer concentration, normalized to the value for untreated cells. All data are means ± SD from 3 biologically independent experiments.

that gapmers against the conserved s2m element or, by extension, other conserved RNA elements may act as viable antiviral agents, warranting their further exploration as therapeutics.

DISCUSSION

For many RNA viruses, genomic RNA structures play critical roles in the replication cycle, including in the modulation of the immune response, regulation of virus RNA replication, virus protein translation, and interactions with host factors. This undoubtedly impacts the evolution of both hosts and viruses, leading to selection and conservation of such structured RNA elements (33). The s2m element, found across different distantly related RNA viruses (10), is a good example of this, although its exact role(s) in the virus life cycle and possible interaction partners are yet to be determined. Nonetheless, the remarkable conservation of the s2m makes it an attractive target for therapeutic intervention, which was explored in this study.

We have confirmed that the s2m element in the 3′ UTR of SARS-CoV-2 RNA is a feasible candidate for ASO-based targeting. For this, we designed and successfully tested LNA-based gapmer ASOs against the s2m. We demonstrated physical gapmer-induced disruption of the RNA structure, consistent with successful gapmer-target base-pairing interactions, and RNase H-induced target degradation *in vitro*. Furthermore, we have demonstrated that the s2m element can direct gapmer-induced reduction of gene expression in GFP reporter assays in human cells, likely relying on the demonstrated enzymatic activity of endogenous RNase H in the nucleus and the cytoplasm (34).

We extended the observation by testing the ability of s2m-targeting gapmers to inhibit viral replication in an astrovirus-based replicon model system, a rapid functional
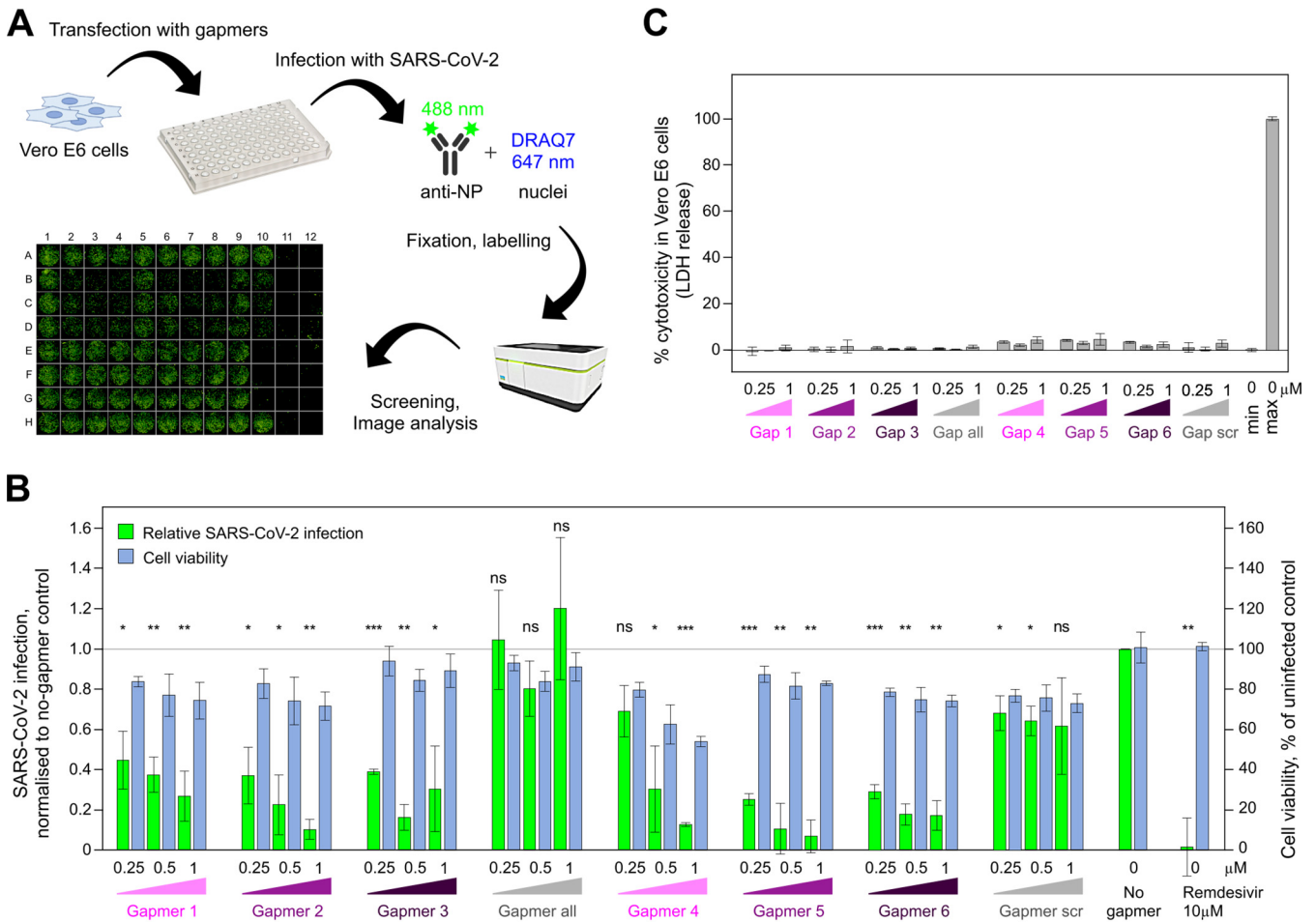
FIG 7 Inhibition of SARS-CoV-2 growth by gapmers targeting the s2m RNA element. (A) Graphic representation of the high-content screening assay experiment workflow: transfection of Vero E6 cells with gapmers followed by infection with SARS-CoV-2, fixation of the plate, labeling, and screening. A representative image from the immunofluorescence-based detection of SARS-CoV-2 infection of Vero E6 cells is shown at the bottom. (B) Vero E6 cells were transfected with gapmers 1 to 6 against the s2m element or control gapmers "all" and "scr" at 0.25 μM, 0.5 μM, and 1 μM final concentrations, infected with SARS-CoV-2, fixed, labeled, and analyzed. Results are presented as means ± SD for 3 biological replicates; signal was normalized to a no-gapmer control. Cell viability was evaluated using the DRAQ7 signal normalized to that in mock-treated wells. P values are from two-tailed t tests with separate variances (ns, not significant [$P > 0.05$]; *, $P \leq 0.05$; **, $P \leq 0.01$; ***, $P \leq 0.001$). (C) Toxicity assay for gapmer-treated Vero E6 cells in the absence of transfection reagent. Cells were treated with 0.25 μM, 0.5 μM, and 1 μM gapmers for 24 h. Supernatant was used to measure cell viability, calculated as the ratio of released to total lactate dehydrogenase (LDH) activity. "max" refers to maximum LDH measured for fully lysed cells.

assay that does not require access to higher-containment-level facilities. Astrovirus replicon assays showed that gapmers against s2m inhibit replication in a sequence-specific, dose-dependent manner, down to the subnanomolar range. These observations confirm that gapmers have significant potential as RNA replication inhibitors. Results from SARS-CoV-2 infection assays in cell culture are also highly encouraging, with inhibition observed at the 0.25 to 1 μM gapmer concentration range. Two of the tested gapmers, 2 and 5, provided consistent inhibition results in both systems without increased cellular toxicity. These gapmer results also highlight specific target regions within the s2m element that could be particularly promising for the development of therapeutic ASOs. In the cellular environment in the replicon assays and in bona fide SARS-CoV-2 infection, the differences in gapmer efficiencies could be attributed to a combination of multiple possible factors, including target sequence accessibility, nuanced differences in the target structure, other multimolecular interactions, and possible off-target effects.

LNA gapmer-based therapies represent an emerging strategy to specifically target RNAs for RNase H-mediated degradation, proven to be a robust pharmacological mechanism in both the cytoplasm and the nucleus (34). More broadly, ASO-based therapies have successfully been applied against myopathies, various genetic disorders, cancers,

and infections with viruses, including cytomegalovirus and Ebola virus (35). With several drug candidates already approved and many in clinical trials, ASO-based therapies represent a promising direction thanks to their high specificity, long-term stability, low toxicity, and relatively low production cost (36).

There are several reports on using ASOs as potential therapeutics against SARS-CoV-2. Of particular interest, a recent study by Sun et al. describes *in vivo* click SHAPE-based detection of functional structured SARS-CoV-2 RNA elements, which are validated by targeting with small interfering RNAs (siRNAs) and ASOs (37). This study highlights the importance of the conserved RNA elements across the coronavirus genome and includes in-depth analyses of conserved RNA elements stem-loop 1 (SL1) to SL4 in the 5′ UTR and SL(ORF10), confirming their potential as antiviral targets. The s2m element has been identified as a discrete structural unit in many studies (6, 15, 23, 37), so it is likely to interact with gapmers similarly in different contexts (reporter, replicon, and virus infection). Targeting UTRs represents a rational way to target both genomic and subgenomic coronavirus RNAs present in the infected cell, hopefully boosting the impact of the therapeutic agent. Further confidence in UTRs as promising therapeutic targets comes from our SARS-CoV-2 gapmer inhibition assay (Fig. 6B), where inhibition is observed for gapmers targeting s2m but not for the gapmer "all," which targets a conserved nonstructural ORF1a region (nt 1359 to 1374), which is present only in the less abundant genomic RNA.

It is worth noting that coronaviruses produce double membrane vesicles inside infected host cells that are thought to conceal the viral double-stranded RNA replicative intermediate from cellular defenses (38, 39). These vesicles have been proposed to be formed through virus-induced manipulations of the membrane of the endoplasmic reticulum (40). This compartmentalization of the SARS-CoV-2 genome in membranous bodies within the host cell cytoplasm (24) may reduce access of the ASOs to the s2m element or other viral genomic targets (although viral mRNAs, which all contain s2m, should still be accessible). In this regard, it is useful to consider that LNA ASOs have been conjugated with tocopherol and cholesterol for membrane association in the past (41, 42), which could increase the ability of ASOs to find their targets. Improved membrane association may also boost gapmer entry into target cells. The primary targets for SARS-CoV-2 infection are the ACE2 receptor-expressing airway cells, with virus infection gradually decreasing from the proximal to distal respiratory tract (43). These cells might be amenable to ASO delivery through aerosol (44), enabling highly targeted therapeutic administration.

When considering s2m as a target for virus inhibition, it is also worth noting that while it is a remarkably stable genomic element, conserved across multiple groups of single-stranded positive-sense RNA viruses, some mutations can arise over time. In the SARS-CoV-2 sequences from COVID-19 patient samples, some s2m polymorphisms and deletions that are predicted to destabilize or disrupt the structure have been detected (11, 12). Using a combination of several gapmers offers a potential therapeutic strategy to guard against emerging resistance.

The results described here represent a promising start for further research into targeting conserved elements in (+)ssRNA viruses and support development of gapmers and related ASOs against the s2m element in particular. In the case of SARS-CoV-2, our gapmer designs offer a strong starting point for further therapeutic development, which may include large-scale optimization and screening to maximize efficacy in cell culture and animal models, as well as chemical modifications for optimal delivery to target cells.

MATERIALS AND METHODS

RNA preparation. 3′ UTRs and the s2m 47-mer were prepared by *in vitro* transcription (IVT). Templates for IVT were generated either by PCR, using Phire Hotstart II polymerase (Thermo Fisher) according to manufacturer's instructions, or by hybridizing cDNA oligonucleotides (Sigma). Sequences for the PCR primers and the DNA oligonucleotides are given in Table 2. RNA generated by IVT was purified: IVT products were separated on polyacrylamide denaturing gel (National Diagnostics), and relevant bands were excised using UV shadowing, electroeluted in Tris-borate-EDTA (TBE) (Whatman Elutrap), and then cleaned up using a PureLink RNA Microscale kit (Invitrogen). RNA concentrations were

TABLE 6 Primers for IVT and SHAPE analysis

Name	Type	Sequence
3′ UTR_F	IVT primer	GTTTTTTAATACGACTCACTATAGCAATCTTTAATCAGTGTGTAACATTAGG
3′ UTR_R	IVT primer	TTTTTTTTTTTTTTTTTTTTTGTCATTCTCCTAAGAAGC
S2M_F	IVT primer	GTTTTTTAATACGACTCACTATAGGAGTTCACCGAGGCCACGCGGAGTAC GATCGAGTGTACAGTGAATT
S2M_R	IVT primer	AATTCACTGTACACTCGATCGTACTCCGCGTGGCCTCGGTGAACTCCTATA GTGAGTCGTATTAAAAAAC
COV19_RT	SHAPE primer	Cy5-CTCTTCCATATAGGCAGCTC

estimated using UV absorbance (A_{260}) and a calculated extinction coefficient. All RNA sequences used in this study are provided in Table 1.

Gel-based RNA cleavage assay. Each gapmer was preincubated with target RNA in 1× RNase H buffer (Thermo Scientific) for 10 min at 37°C. Then, 2.5 U of RNase H (Thermo Scientific) was added, and the reaction mixture was incubated for 20 min at 37°C. Reactions were quenched by adding an equal volume of proteinase K mix (0.5 mg/ml enzyme, 100 mM Tris-HCl [pH 7.5], 150 mM NaCl, 12.5 mM EDTA, 1% [wt/vol] SDS) and incubating at 50°C for 20 min. RNA was visualized on polyacrylamide–7.5 M urea gels (National Diagnostics) in TBE using SybrGold (Invitrogen).

Chemical probing of the 3′ UTR. To probe RNA structure without gapmers, 5 pmol RNA (~350 ng) was dissolved in 9 μl nuclease-free water, denatured at 95°C for 90 s, and then cooled on ice for 2 min. RNA was refolded by adding 10 μl of 2× SHAPE probing buffer (80 mM HEPES [pH 7.5], 200 mM KCl, 1 mM MgCl$_2$) and incubating at 37°C for 15 min. 2-Methylnicotinic acid imidazolide (NAI) was added to a final concentration of 100 mM in a 20-μl reaction mixture; for control reactions, the same volume of dimethyl sulfoxide (DMSO) was added instead. Reactions were allowed to proceed at 37°C for 5 min and then quenched by adding 10 μl of 2 M dithiothreitol (DTT). RNA was purified by loading quenched samples onto Micro Bio-spin columns with Bio-Gel P-6 (Bio-Rad), followed by ethanol precipitation. Purified RNA was then dissolved in 6 μl water, reverse transcribed to cDNA, and analyzed by PAGE as described below.

To probe RNA structure with gapmers, different amounts of gapmers were added to refolded RNA, at molar ratios of 0.5×, 1×, or 2×, and incubated at 37°C for 10 min. The same volume of water was added for the no-gapmer control. After coincubation, RNA was probed using NAI as described above. In addition, unprobed input RNA was also subjected to Sanger sequencing: RNA was dissolved in 5 μl water, supplemented with 1 μl of a 10 mM concentration of the corresponding dideoxynucleoside triphosphate (ddNTP) (Roche), then reverse-transcribed to cDNA, and analyzed by PAGE as described below.

Reverse transcription and PAGE analysis of cDNA. A 6-μl portion of each RNA-containing sample was mixed with 1 μl of 5 μM Cy5-modified reverse transcription (RT) primer (sequence given in Table 6) and 0.5 μl of 10 mM dNTPs. The mixture was incubated at 95°C for 3 min to denature the RNA and then cooled to 50°C. The RT reaction was started by adding 2 μl of 5× RT buffer (100 mM Tris [pH 8.3], 500 mM LiCl, 15 mM MgCl$_2$, 5 mM DTT) and 0.5 μl Superscript III enzyme (Invitrogen) and mixing quickly with a pipette tip. The reaction was allowed to proceed at 50°C for 20 min and then quenched by incubation at 85°C for 10 min, which inactivates the enzyme. In order to degrade RNA and liberate the complementary cDNA, the reaction mixture was then supplemented with 0.5 μl of 2 M NaOH and incubated at 95°C for 10 min. The reaction was stopped by adding an equal volume of 2× stopping buffer (95% formaldehyde, 20 mM EDTA [pH 8.0], 20 mM Tris-HCl [pH 7.5], orange G dye) and incubating at 95°C for 5 min. The resulting cDNA sample was cooled to 65°C and analyzed on an 8% acrylamide–bis-acrylamide–urea gel by electrophoresis. The gel was imaged with a Typhoon FLA 9000 gel imager (GE Healthcare).

Quantitative gel analysis and SHAPE reactivity calculation. Signal intensity of each band on the PAGE gel was detected using ImageQuant TL software and normalized to the total signal of the whole lane. Raw reactivity was generated by subtracting the signal of NAI channel from that of the DMSO control channel; reactivities with negative values were corrected to 0. SHAPE reactivity was generated following the 2/8% normalization method (45). To calculate the differences in SHAPE signal in the presence and absence of gapmers, the lanes of NAI channels with 2× gapmer (+gapmer) or without gapmer (−gapmer) were used. The signal intensity of each band was normalized to the total signal of the whole lane. Differences were calculated by subtracting the signal of the +gapmer channel from that of the −gapmer channel and then rescaled to the signal of the −gapmer channel.

Cryo-electron microscopy. A 5 μM concentration of purified 3′ UTR in 10 mM Tris (pH 7.6)–10 mM KCl–10 mM NaCl was annealed by sequential incubation at 95°C for 2 min, at 50°C for 2 min, at 37°C for 5 min, and then at room temperature. The sample was supplemented with 1 mM MgCl$_2$, and 3 μl of the resultant mixture was applied to glow-discharged (EasiGlow Pelco) R2/2 Quantifoil grids (Quantifoil). Excess sample was blotted away with a FEI Vitrobot (IV) (100% humidity; 4°C; blotting force, 0; 3-s blot time) and the grids were vitrified in liquid ethane. The grids were screened with a 200-kV FEI Talos Arctica microscope with a Falcon III camera, and a data set was collected on a 300-kV FEI Titan Krios microscope equipped with a Gatan K3 camera. Motion correction, contrast transfer function (CTF) estimation, and particle picking were performed in Warp (46), and 2D/3D alignments and averaging were carried out with cryoSPARC 2.15 (47). All cryo-EM grids were prepared and cryo-EM data collected at the BIOCEM facility, Department of Biochemistry, University of Cambridge.

Gapmer reporter assays. The s2m sequence or control scrambled sequence of s2m (s2m_scr) was inserted into the 3′ UTR of GFP in the H6P plasmid using an In-Fusion cloning kit (TaKaRa) and verified

by sequencing. HEK293ET, HeLa, and A459 cells, as well as all stable cell lines, were grown in Iscove's modified Dulbecco's medium (IMDM) supplemented with 10% fetal calf serum (FCS) at 37°C in 5% CO_2. All cell lines tested negative for mycoplasma. Constructs in H6P plasmids were used to produce recombinant lentivirus in HEK293ET cells for the stable expression of GFP reporter in mammalian cells from a constitutive spleen focus-forming virus (SFFV) promoter. HeLa and A549 stable cell lines were generated by lentiviral transduction with a low multiplicity of infection (MOI) ($>$0.3) to ensure single genomic integrations and were selected for by drug resistance.

To examine the effect of gapmers on GFP expression, HeLa or A549 cells with a stably integrated GFP-s2m/s2m_scr reporter were seeded at 5×10^4 cells per well in 24-well plates. The following day, cells were transfected with gapmer to achieve a 20 nM final concentration using Lipofectamine RNAiMAX (Thermo Fisher Scientific). Flow cytometry analysis was performed 72 h after transfection. Cells were washed twice with warm phosphate-buffered saline (PBS), detached with trypsin, and resuspended in IMDM. All samples were analyzed on a BD LSR II flow cytometer, using the high-throughput system (HTS), and at least 20,000 events were acquired for each sample. Data were analyzed in FlowJo (v10.7.1). The main cell population was identified and gated on forward and side scatter using the Auto Gate tool and plotted as a histogram to visualize GFP intensity of cells (measured using a B-525 detector).

Virus replicon assays. HEK293T cells (ATCC) were maintained at 37°C in DMEM supplemented with 10% fetal bovine serum (FBS), 1 mM L-glutamine, and antibiotics. Huh7.5.1 cells (Apath, Brooklyn, NY) (48) were maintained in the same medium supplemented with nonessential amino acids. All cells were mycoplasma tested (MycoAlert Plus assay; Lonza); Huh7.5.1 cells were also tested by deep sequencing.

The HAstV1 replicon system is based on the HAstV1 infectious clone, where the virus genome is left intact up to the end of ORFX and then followed by a foot-and-mouth disease virus 2A sequence and a *Renilla* luciferase (RLuc) sequence fused in the ORF2 reading frame, followed by the last 624 nt of the virus genome and a poly(A) tail (Fig. 4A) (GenBank accession number MN030571) (29). The s2m mutations were introduced using site-directed mutagenesis, and all constructs were confirmed by sequencing. The resulting plasmids were linearized with XhoI prior to T7 RNA transcription.

Huh7.5.1 and HEK293T cells were transfected in triplicate with Lipofectamine 2000 reagent (Invitrogen), using the protocol in which suspended cells are added directly to the RNA complexes in 96-well plates. For each transfection, 100 ng replicon, 10 ng firefly luciferase-encoding purified T7 RNA (RNA Clean and Concentrator; Zymo Research), the indicated amount of gapmers, and 0.3 μl Lipofectamine 2000 in 20 μl Opti-MEM (Gibco) supplemented with RNaseOUT (Invitrogen; diluted 1:1,000 in Opti-MEM) were added to each well containing 5×10^4 cells in 100 μl DMEM supplemented with 5% FBS, and wells were incubated at 37°C for 12 h (Huh7.5.1) or 18 h (HEK293T). Firefly and *Renilla* luciferase activities were determined using the dual-luciferase Stop & Glo reporter assay system (Promega). Replicon activity was calculated as the ratio of *Renilla* (subgenomic reporter) to firefly (cap-dependent translation, loading control) luciferase activity, normalized by the same ratio for the control replicon, as indicated for each experiment. Three independent experiments, each in triplicate, were performed to confirm reproducibility of results.

Cytotoxicity assays. The analysis of gapmer cytotoxicity in HEK293T, Huh7.5.1, and Vero E6 cells was performed using the CyQUANT LDH cytotoxicity assay (Thermo Scientific). Leaked cytoplasmic LDH in cell culture supernatants was quantified after enzymatic conversion, and absorbance was measured at 490 nm in a 96-well plate reader according to the manufacturer's instructions.

SARS-CoV-2 production and infection. Vero E6 cells obtained from Oliver Schwarz (Institute Pasteur, Paris) were maintained in DMEM modified with high glucose, L-glutamine, phenol red, and sodium pyruvate (Thermo Fisher number 41966-029) supplemented with 10% FCS at 5% CO_2. SARS-CoV-2 strain BetaCoV/England/02/2020 (obtained from Public Health England) was propagated at 37°C on Vero E6 cells in DMEM supplemented with 10% FCS at 37°C. The titer was determined by plaque assay as follows. Confluent monolayers of VeroE6 cells were grown on 6-well plates and incubated with 200 μl of a 10-fold serial dilution of virus stock in DMEM supplemented with 10% FCS for 1 h at room temperature. These cells were then overlaid with 0.5$\times$ DMEM supplemented with 1% FCS and 1.2% Avicel (BMC Biopolymers, Belgium). After 4 days incubation at 37°C, cells were fixed with 4% formaldehyde in PBS followed by staining with 0.1% toluidine blue (Sigma number 89640). The titer was calculated as PFU per milliliter.

SARS-CoV-2 infection assay. Vero E6 cells (National Institute for Biological Standards and Control [NIBSC], UK) were grown in DMEM (containing 10% FBS) at 37°C and 5% CO_2 in 96-well imaging plates (Greiner 655090). Cells were transfected with individual gapmers at a 0.25, 0.5 or 1 μM final concentration using Lipofectamine 2000 (Thermo Fisher), according to the manufacturer's instructions. At 6 h posttransfection, the medium was replaced, and the cells were infected with SARS-CoV-2 at a multiplicity of infection of 0.5 PFU/cell or mock infected. At 22 h postinfection, cells were fixed, permeabilized, and stained for SARS-CoV-2 N protein using Alexa Fluor 488-labeled-CR3009 antibody (49) and for nuclei (DRAQ7; 647-nm wavelength). The plate was imaged using the high-content screening microscope Opera Phenix from Perkin Elmer with a 5$\times$ lens. The Opera Phenix-associated software Harmony was used to delineate the whole well area and to determine the total intensities of the Alexa Fluor 488-N protein and DRAQ7-DNA signals per said whole well area during image acquisition. The background-subtracted Alexa Fluor 488-N intensities were normalized to vehicle-treated samples. Toxicity was evaluated using the DRAQ7-DNA signal normalized to mock-treated wells and LDH release-based cytotoxicity assay.

REFERENCES

1. Messner CB, Demichev V, Wendisch D, Michalick L, White M, Freiwald A, Textoris-Taube K, Vernardis SI, Egger AS, Kreidl M, Ludwig D, Kilian C, Agostini F, Zelezniak A, Thibeault C, Pfeiffer M, Hippenstiel S, Hocke A, von Kalle C, Campbell A, Hayward C, Porteous DJ, Marioni RE, Langenberg C, Lilley KS, Kuebler WM, Mülleder M, Drosten C, Suttorp N, Witzenrath M, Kurth F, Sander LE, Ralser M. 2020. Ultra-high-throughput clinical proteomics reveals classifiers of COVID-19 infection. Cell Syst 11:11–24.E4. https://doi.org/10.1016/j.cels.2020.05.012.

2. Koirala A, Joo YJ, Khatami A, Chiu C, Britton PN. 2020. Vaccines for COVID-19: the current state of play. Paediatr Respir Rev 35:43–49. https://doi.org/10.1016/j.prrv.2020.06.010.

3. Krammer F. 2020. SARS-CoV-2 vaccines in development. Nature 586:516–527. https://doi.org/10.1038/s41586-020-2798-3.

4. Menachery VD, Yount BL, Debbink K, Agnihothram S, Gralinski LE, Plante JA, Graham RL, Scobey T, Ge XY, Donaldson EF, Randell SH, Lanzavecchia A, Marasco WA, Shi ZL, Baric RS. 2015. A SARS-like cluster of circulating bat coronaviruses shows potential for human emergence. Nat Med 21:1508–1513. https://doi.org/10.1038/nm.3985.

5. Akula SM, McCubrey JA. 2020. Where are we with understanding of COVID-19? Adv Biol Regul 78:100738. https://doi.org/10.1016/j.jbior.2020.100738.

6. Rangan R, Zheludev IN, Hagey RJ, Pham EA, Wayment-Steele HK, Glenn JS, Das R. 2020. RNA genome conservation and secondary structure in SARS-CoV-2 and SARS-related viruses: a first look. RNA 26:937–959. https://doi.org/10.1261/rna.076141.120.

7. Kim D, Lee JY, Yang JS, Kim JW, Kim VN, Chang H. 2020. The architecture of SARS-CoV-2 transcriptome. Cell 181:914–921.E10. https://doi.org/10.1016/j.cell.2020.04.011.

8. Jonassen CM, Jonassen T, Grinde B. 1998. A common RNA motif in the 3' end of the genomes of astroviruses, avian infectious bronchitis virus and an equine rhinovirus. J Gen Virol 79:715–718. https://doi.org/10.1099/0022-1317-79-4-715.

9. Tengs T, Kristoffersen AB, Bachvaroff TR, Jonassen CM. 2013. A mobile genetic element with unknown function found in distantly related viruses. Virol J 10:132. https://doi.org/10.1186/1743-422X-10-132.

10. Tengs T, Jonassen C. 2016. Distribution and evolutionary history of the mobile genetic element s2m in coronaviruses. Diseases 4:27. https://doi.org/10.3390/diseases4030027.

11. Vahed M, Vahed M, Sweeney A, Shirazi FH, Mirsaeidi M. 2020. Mutation in position of 32 (G>U) of S2M differentiate human SARS-CoV2 from bat coronavirus. bioRxiv https://doi.org/10.1101/2020.09.02.280529.

12. Yeh TY, Contreras GP. 2020. Emerging viral mutants in Australia suggest RNA recombination event in the SARS-CoV-2 genome. Med J Aust 213:44–44.E1. https://doi.org/10.5694/mja2.50657.

13. Robertson MP, Igel H, Baertsch R, Haussler D, Ares M, Scott WG. 2005. The structure of a rigorously conserved RNA element within the SARS virus genome. PLoS Biol 3:e5. https://doi.org/10.1371/journal.pbio.0030005.

14. Huston NC, Wan H, Strine MS, de Cesaris Araujo Tavares R, Wilen CB, Pyle AM. 2021. Comprehensive in vivo secondary structure of the SARS-CoV-2 genome reveals novel regulatory motifs and mechanisms. Mol Cell 81:584–598.E5. https://doi.org/10.1016/j.molcel.2020.12.041.

15. Ziv O, Price J, Shalamova L, Kamenova T, Goodfellow I, Weber F, Miska EA. 2020. The short- and long-range RNA-RNA interactome of SARS-CoV-2. Mol Cell 80:1067–1077.E5. https://doi.org/10.1016/j.molcel.2020.11.004.

16. Bennett CF. 2019. Therapeutic antisense oligonucleotides are coming of age. Annu Rev Med 70:307–321. https://doi.org/10.1146/annurev-med-041217-010829.

17. Singh SK, Nielsen P, Koshkin AA, Wengel J. 1998. LNA (locked nucleic acids): synthesis and high-affinity nucleic acid recognition. Chem Commun (Camb) 1998:455–456. https://doi.org/10.1039/a708608c.

18. Hagedorn PH, Persson R, Funder ED, Albæk N, Diemer SL, Hansen DJ, Møller MR, Papargyri N, Christiansen H, Hansen BR, Hansen HF, Jensen MA, Koch T. 2018. Locked nucleic acid: modality, diversity, and drug discovery. Drug Discov Today 23:101–114. https://doi.org/10.1016/j.drudis.2017.09.018.

19. Wahlestedt C, Salmi P, Good L, Kela J, Johnsson T, Hökfelt T, Broberger C, Porreca F, Lai J, Ren K, Ossipov M, Koshkin A, Jakobsen N, Skouv J, Oerum H, Jacobsen MH, Wengel J. 2000. Potent and nontoxic antisense oligonudeotides containing locked nucleic acids. Proc Natl Acad Sci U S A 97:5633–5638. https://doi.org/10.1073/pnas.97.10.5633.

20. Bonneau E, Neveu B, Kostantin E, Tsongalis GJ, De Guire V. 2019. How close are miRNAs from clinical practice? A perspective on the diagnostic and therapeutic market. EJIFCC 40:114–127.

21. Wacker A, Weigand JE, Akabayov SR, Altincekic N, Bains JK, Banijamali E, Binas O, Castillo-Martinez J, Cetiner E, Ceylan B, Chiu LY, Davila-Calderon J, Dhamotharan K, Duchardt-Ferner E, Ferner J, Frydman L, Fürtig B, Gallego J, Tassilo Grün J, Hacker C, Haddad C, Hähnke M, Hengesbach M, Hiller F, Hohmann KF, Hymon D, de Jesus V, Jonker H, Keller H, Knezic B, Landgraf T, Löhr F, Luo L, Mertinkus KR, Muhs C, Novakovic M, Oxenfarth A, Palomino-Schätzlein M, Petzold K, Peter SA, Pyper DJ, Qureshi NS, Riad M, Richter C, Saxena K, Schamber T, Scherf T, Schlagnitweit J, Schlundt A, Schnieders R, et al. 2020. Secondary structure determination of conserved SARS-CoV-2 RNA elements by NMR spectroscopy. Nucleic Acids Res 48:12415–12435. https://doi.org/10.1093/nar/gkaa1013.

22. Spitale RC, Crisalli P, Flynn RA, Torre EA, Kool ET, Chang HY. 2013. RNA SHAPE analysis in living cells. Nat Chem Biol 9:18–20. https://doi.org/10.1038/nchembio.1131.

23. Manfredonia I, Nithin C, Ponce-Salvatierra A, Ghosh P, Wirecki TK, Marinus T, Ogando NS, Snijder EJ, van Hemert MJ, Bujnicki JM, Incarnato D. 2020. Genome-wide mapping of SARS-CoV-2 RNA structures identifies therapeutically-relevant elements. Nucleic Acids Res 48:12436–12452. https://doi.org/10.1093/nar/gkaa1053.

24. Klein S, Cortese M, Winter SL, Wachsmuth-Melm M, Neufeldt CJ, Cerikan B, Stanifer ML, Boulant S, Bartenschlager R, Chlanda P. 2020. SARS-CoV-2 structure and replication characterized by in situ cryo-electron tomography. Nat Commun 11:5885. https://doi.org/10.1038/s41467-020-19619-7.

25. Kumar R, Singh SK, Koshkin AA, Rajwanshi VK, Meldgaard M, Wengel J. 1998. The first analogues of LNA (locked nucleic acids): phosphorothioate-LNA and 2'-thio-LNA. Bioorganic Med Chem Lett 8:2219–2222. https://doi.org/10.1016/S0960-894X(98)00366–7.

26. Eckstein F. 2000. Phosphorothioate oligodeoxynucleotides: what is their origin and what is unique about them? Antisense Nucleic Acids Drug Dev 10:117–121. https://doi.org/10.1089/oli.1.2000.10.117.

27. Grünweller A, Wyszko E, Bieber B, Jahnel R, Erdmann VA, Kurreck J. 2003. Comparison of different antisense strategies in mammalian cells using locked nucleic acids, 2′-O-methyl RNA, phosphorothioates and small interfering RNA. Nucleic Acids Res 31:3185–3193. https://doi.org/10.1093/nar/gkg409.

28. Kurreck J, Wyszko E, Gillen C, Erdmann VA. 2002. Design of antisense oligonucleotides stabilized by locked nucleic acids. Nucleic Acids Res 30:1911–1918. https://doi.org/10.1093/nar/30.9.1911.

29. Lulla V, Firth AE. 2020. A hidden gene in astroviruses encodes a viroporin. Nat Commun 11:4070. https://doi.org/10.1038/s41467-020-17906-x.

30. Aldhumani AH, Hossain MI, Fairchild EA, Boesger H, Marino EC, Myers M, Hines JV. 2021. RNA sequence and ligand binding alter conformational profile of SARS-CoV-2 stem loop II motif. Biochem Biophys Res Commun 545:75–80. https://doi.org/10.1016/j.bbrc.2021.01.013.

31. Kaur H, Babu BR, Maiti S. 2007. Perspective on chemistry and therapeutic applications of locked nucleic acid (LNA). Chem Rev 107:4672–4697. https://doi.org/10.1021/cr050266u.

32. Fazil MHUT, Ong ST, Chalasani MLS, Low JH, Kizhakeyil A, Mamidi A, Lim CFH, Wright GD, Lakshminarayanan R, Kelleher D, Verma NK. 2016. GapmeR cellular internalization by macropinocytosis induces sequence-specific gene silencing in human primary T-cells. Sci Rep 6:37721. https://doi.org/10.1038/srep37721.

33. Smyth RP, Negroni M, Lever AM, Mak J, Kenyon JC. 2018. RNA structure—a neglected puppet master for the evolution of virus and host immunity. Front Immunol 9:2097. https://doi.org/10.3389/fimmu.2018.02097.

34. Liang XH, Sun H, Nichols JG, Crooke ST. 2017. RNase H1-dependent antisense oligonucleotides are robustly active in directing RNA cleavage in both the cytoplasm and the nucleus. Mol Ther 25:2075–2092. https://doi.org/10.1016/j.ymthe.2017.06.002.

35. Berber B, Aydin C, Kocabas F, Guney-Esken G, Yilancioglu K, Karadag-Alpaslan M, Caliseki M, Yuce M, Demir S, Tastan C. 2020. Gene editing and RNAi approaches for COVID-19 diagnostics and therapeutics. Gene Ther https://doi.org/10.1038/s41434-020-00209-7.

36. Crooke ST, Witztum JL, Bennett CF, Baker BF. 2018. RNA-targeted therapeutics. Cell Metab 27:714–739. https://doi.org/10.1016/j.cmet.2018.03.004.

37. Sun L, Li P, Ju X, Rao J, Huang W, Ren L, Zhang S, Xiong T, Xu K, Zhou X, Gong M, Miska E, Ding Q, Wang J, Zhang QC. 2021. In vivo structural characterization of the SARS-CoV-2 RNA genome identifies host proteins vulnerable to repurposed drugs. Cell 184:1865–1883.E20. https://doi.org/10.1016/j.cell.2021.02.008.

38. Hagemeijer MC, Vonk AM, Monastyrska I, Rottier PJM, de Haan CAM. 2012. Visualizing coronavirus RNA synthesis in time by using click chemistry. J Virol 86:5808–5816. https://doi.org/10.1128/JVI.07207–11.

39. Knoops K, Kikkert M, Van Den Worm SHE, Zevenhoven-Dobbe JC, Van Der Meer Y, Koster AJ, Mommaas AM, Snijder EJ. 2008. SARS-coronavirus replication is supported by a reticulovesicular network of modified endoplasmic reticulum. PLoS Biol 6:e226. https://doi.org/10.1371/journal.pbio.0060226.

40. Blanchard E, Roingeard P. 2015. Virus-induced double-membrane vesicles. Cell Microbiol 17:45–50. https://doi.org/10.1111/cmi.12372.

41. Benizri S, Gissot A, Martin A, Vialet B, Grinstaff MW, Barthélémy P. 2019. Bioconjugated oligonucleotides: recent developments and therapeutic applications. Bioconjug Chem 30:366–383. https://doi.org/10.1021/acs.bioconjchem.8b00761.

42. Nishina T, Numata J, Nishina K, Yoshida-Tanaka K, Nitta K, Piao W, Iwata R, Ito S, Kuwahara H, Wada T, Mizusawa H, Yokota T. 2015. Chimeric antisense oligonucleotide conjugated to α-tocopherol. Mol Ther Nucleic Acids 4:e220. https://doi.org/10.1038/mtna.2014.72.

43. Hou YJ, Okuda K, Edwards CE, Martinez DR, Asakura T, Dinnon KH, Kato T, Lee RE, Yount BL, Mascenik TM, Chen G, Olivier KN, Ghio A, Tse LV, Leist SR, Gralinski LE, Schäfer A, Dang H, Gilmore R, Nakano S, Sun L, Fulcher ML, Livraghi-Butrico A, Nicely NI, Cameron M, Cameron C, Kelvin DJ, de Silva A, Margolis DM, Markmann A, Bartelt L, Zumwalt R, Martinez FJ, Salvatore SP, Borczuk A, Tata PR, Sontake V, Kimple A, Jaspers I, O'Neal WK, Randell SH, Boucher RC, Baric RS. 2020. SARS-CoV-2 reverse genetics reveals a variable infection gradient in the respiratory tract. Cell 182:429–446.e14. https://doi.org/10.1016/j.cell.2020.05.042.

44. Drevinek P, Pressler T, Cipolli M, De Boeck K, Schwarz C, Bouisset F, Boff M, Henig N, Paquette-Lamontagne N, Montgomery S, Perquin J, Tomkinson N, den Hollander W, Elborn JS. 2020. Antisense oligonucleotide eluforsen is safe and improves respiratory symptoms in F508DEL cystic fibrosis. J Cyst Fibros 19:99–107. https://doi.org/10.1016/j.jcf.2019.05.014.

45. Low JT, Weeks KM. 2010. SHAPE-directed RNA secondary structure prediction. Methods 52:150–158. https://doi.org/10.1016/j.ymeth.2010.06.007.

46. Tegunov D, Cramer P. 2019. Real-time cryo-electron microscopy data preprocessing with Warp. Nat Methods 16:1146–1152. https://doi.org/10.1038/s41592-019-0580-y.

47. Punjani A, Rubinstein JL, Fleet DJ, Brubaker MA. 2017. CryoSPARC: algorithms for rapid unsupervised cryo-EM structure determination. Nat Methods 14:290–296. https://doi.org/10.1038/nmeth.4169.

48. Zhong J, Gastaminza P, Cheng G, Kapadia S, Kato T, Burton DR, Wieland SF, Uprichard SL, Wakita T, Chisari FV. 2005. Robust hepatitis C virus infection in vitro. Proc Natl Acad Sci U S A 102:9294–9299. https://doi.org/10.1073/pnas.0503596102.

49. van den Brink EN, ter Meulen J, Cox F, Jongeneelen MAC, Thijsse A, Throsby M, Marissen WE, Rood PML, Bakker ABH, Gelderblom HR, Martina BE, Osterhaus ADME, Preiser W, Doerr HW, de Kruif J, Goudsmit J. 2005. Molecular and biological characterization of human monoclonal antibodies binding to the spike and nucleocapsid proteins of severe acute respiratory syndrome coronavirus. J Virol 79:1635–1644. https://doi.org/10.1128/JVI.79.3.1635-1644.2005.